Bioactive Materials 36 (2024) 168–184

Contents lists available at ScienceDirect

Bioactive Materials

journal homepage: www.keaipublishing.com/en/journals/bioactive-materials

Advanced PEG-tyramine biomaterial ink for precision engineering of perfusable and flexible small-diameter vascular constructs via coaxial printing

Julia Simińska-Stanny [a], Lise Nicolas [a,b], Adam Chafai [c], Hafez Jafari [a], Maryam Hajiabbas [a,f], Gianina Dodi [d], Ioannis Gardikiotis [e], Christine Delporte [f], Lei Nie [a,g,***], Daria Podstawczyk [h,**], Amin Shavandi [a,*]

[a] Université Libre de Bruxelles (ULB), École polytechnique de Bruxelles, 3BIO-BioMatter, Avenue F.D. Roosevelt, 50 - CP 165/61, 1050, Brussels, Belgium
[b] European School of Materials Science and Engineering, University of Lorraine, Nancy, France
[c] Université Libre de Bruxelles (ULB), Micro-milli Platform, Avenue F.D. Roosevelt, 50 - CP 165/67, 1050, Brussels, Belgium
[d] Faculty of Medical Bioengineering, Grigore T. Popa, University of Medicine and Pharmacy of Iasi, Romania
[e] Advanced Research and Development Center for Experimental Medicine, Grigore T. Popa, University of Medicine and Pharmacy of Iasi, Romania
[f] Université Libre de Bruxelles (ULB), Faculté de Médecine, Campus Erasme - CP 611, Laboratory of Pathophysiological and Nutritional Biochemistry, Route de Lennik, 808, 1070, Bruxelles, Belgium
[g] College of Life Science, Xinyang Normal University, Xinyang, China
[h] Department of Process Engineering and Technology of Polymer and Carbon Materials, Faculty of Chemistry, Wroclaw University of Science and Technology, Norwida 4/6, 50-373, Wroclaw, Poland

A B S T R A C T

Vascularization is crucial for providing nutrients and oxygen to cells while removing waste. Despite advances in 3D-bioprinting, the fabrication of structures with void spaces and channels remains challenging. This study presents a novel approach to create robust yet flexible and permeable small (600–1300 μm) artificial vessels in a single processing step using 3D coaxial extrusion printing of a biomaterial ink, based on tyramine-modified polyethylene glycol (PEG-Tyr). We combined the gelatin biocompatibility/activity, robustness of PEG-Tyr and alginate with the shear-thinning properties of methylcellulose (MC) in a new biomaterial ink for the fabrication of bioinspired vessels. Chemical characterization using NMR and FTIR spectroscopy confirmed the successful modification of PEG with Tyr and rheological characterization indicated that the addition of PEG-Tyr decreased the viscosity of the ink. Enzyme-mediated crosslinking of PEG-Tyr allowed the formation of covalent crosslinks within the hydrogel chains, ensuring its stability. PEG-Tyr units improved the mechanical properties of the material, resulting in stretchable and elastic constructs without compromising cell viability and adhesion. The printed vessel structures displayed uniform wall thickness, shape retention, improved elasticity, permeability, and colonization by endothelial-derived - EA.hy926 cells. The chorioallantoic membrane (CAM) and *in vivo* assays demonstrated the hydrogel's ability to support neoangiogenesis. The hydrogel material with PEG-Tyr modification holds promise for vascular tissue engineering applications, providing a flexible, biocompatible, and functional platform for the fabrication of vascular structures.

1. Introduction

Vascularization ensures cells receive nutrients and oxygen while removing metabolic waste. However, achieving proper tissue vascularization remains one of the primary challenges in tissue engineering [1]. Most current approaches still rely on pre-existing blood vessels to grow into the engineered tissue, which limits the size and complexity of the constructs. The arterio-venous loop (AVL) is a promising method investigated for connecting implanted blood vessels to the host's vascular system [2]. However, its effectiveness is limited in tissues with densely packed capillaries [3]. Alternatively, *in vitro* vascularization strategies can be used. Several approaches including channel molding, cell sheet folding, the use of the fugitive ink and electrospinning have been proposed to fabricate small-diameter vessels [4].

Advantages of 3D printing for vascular constructs include the ability to create complex, patient-specific geometries, mimic the intricate

Peer review under responsibility of KeAi Communications Co., Ltd.
* Corresponding author.
** Corresponding author.
*** Corresponding author.
E-mail addresses: nielei@xynu.edu.cn (L. Nie), daria.podstawczyk@pwr.edu.pl (D. Podstawczyk), amin.shavandi@ulb.be (A. Shavandi).

https://doi.org/10.1016/j.bioactmat.2024.02.019
Received 4 October 2023; Received in revised form 9 February 2024; Accepted 16 February 2024

vascular network, facilitate the integration of multiple cell types, and promote functional vascularization [5,6]. Perfusion is essential to secure the survival of tissue grafts and various 3D fabrication strategies have been developed for this purpose. Stereolithography-based 3D printing has been employed to create complex hollow networks by selectively curing photo-crosslinkable hydrogels. For instance, digital light processing (DLP) - based bioprinting can create functional vascular topologies utilizing photo-curable polyethylene glycol diacrylate (PEGDA) hydrogels [7]. 3D extrusion printing has the capacity to construct hydrogel channels with an emphasis on regularity and designed model fidelity [8].

The application of extrusion printing or pore-forming printing for sacrificial filaments of gelatin, agarose or Pluronic F127, has been widely utilized to create open channels within hydrogel matrices. This method facilitates the fabrication of vessel-like structures [9,10,11]. For the creation of microchannels, Kawara et al. used microwires that create precise microchannel patterns mimicking the size of capillaries [12]. While vessel-mimicking structures are fabricated, subsequent post-fabrication steps [13] such as dissolution or removal of the mold are required. Moreover, the intricate nature of sacrificial structure creation imposes constraints on the size and shape of the vessels [14]. In contrast, the 3D coaxial printing method offers the advantage of straightforward control over vessel dimensions through basic adjustments of printing parameters such as material flow rate and nozzle size [13,15]. Several studies have reported successful coaxial printing of tubular structures that replicate blood vessels using various biopolymers such as gelatin and alginate (Alg) [16,17]. The methacrylated gelatin-alginate (GelMA-Alg) microfibers encapsulating endothelial cells (ECs) could form a vasculature-like structure [18]. However, the materials comprising GelMA or Alg showed low flexibility [19]. A few studies have focused on the development of flexible blood vessel grafts and most of them cover the fabrication of larger (>2 mm) vascular grafts [20,21] with the persistence of issues related to flexibility and limitation in the fabrication of vessels <1 mm in diameter. For instance, Carrabba et al. used the electrospinning technique to design a multilayer vessel structure, but despite promising results, the vessels had a diameter >5 mm [22]. Kaufmann et al. employed flexible resin and used stereolithography to fabricate vascular grafts, though they did not reported biocompatibility and endothelialization potential of the constructs [20]. Molding technique in custom-prepared Teflon molds was also used to obtain stable bilayer hydrogel tubes, however with internal diameters of 1.5 mm and larger [23]. Hann et al. achieved biomimetic, flexible vessels by combining fused deposition modeling (FDM) printing with coaxial printing [24], yet, this multistep process remained challenging and could not produce channels with diameter below 2 mm. Another group utilized decellularized aorta ink and extrusion printing for flexible vessels, but faced limitations in achieving structure below 10 mm in diameter [21]. Improvement in vessel elasticity was explored by combining GelMA with alginate dual-network [16,25], suggesting the inadequacy of pure GelMA hydrogels [26]. Studies highlighting improved mechanical properties in fabricated vascular grafts [20,24] often involve materials with inferior biocompatibility [27] or require the incorporation of additional materials into the GelMA chain for the robustness of the construct [28]. For example, the combination of GelMA and poly (ethylene glycol) (PEG) enhances mechanical properties, i.e., compressive modulus and printability compared to individual PEG and GelMA hydrogels [29,26]. The interplay between ionically crosslinked alginate and covalently crosslinked GelMA was used to adjust the mechanical and rheological properties of hydrogels [30].

This study aims to create a hydrogel formulation for fabricating flexible and permeable small-diameter vessels. By combining the viscoelastic properties and cell interactions of gelatin and alginate with the elastic properties of PEG, we aim to bridge the gap between capillaries in the micron range and arteries/veins measuring at least 1 mm in diameter [31]. In our hydrogels, PEG-tyramine undergoes enzymatic crosslinking, forming covalent bonds with tyramine residues at the ends of PEG-chains. This covalent integration enhances the structural stability and mechanical properties of the hydrogel, accounting for enhanced elasticity and flexibility. PEG-tyramine and GelMA also introduce covalent crosslinks within the alginate matrix through enzymatic and photo-mediated reactions, offering a dual (covalent-ionic) crosslinking strategy. Besides, the addition of PEG-tyramine further enhances biocompatibility and may improve the overall performance of the GelMA-based hydrogel [32,33]. We have designed a prototype vessel system using a single processing step of coaxial printing and a tailored PEG-Tyr bioink, resulting in flexible, self-supporting, perfusable vascular models. We investigated vessels' perfusion, permeability, and colonization by ECs.

2. Experimental section

2.1. Materials

Gelatin from porcine skin (type A, gel strength 300 bloom), sodium alginate (Alg – alginic acid sodium salt from brown algae, with a molecular weight of 120–190 kDa), phosphate-buffered saline (PBS), Methacrylic anhydride (MA), Sodium persulfate (SPS), hydrogen peroxide (H_2O_2), horseradish peroxidase (HRP, 271 U/mg) and fluorescein isothiocyanate–dextran (FITC–Dextran, MW 70 000) were purchased from Sigma-Aldrich (St. Louis, MO, USA). Deuterium oxide (D_2O) was purchased from Tokyo Chemical Industry (Tokyo, Japan). Riboflavin 5′-monophosphate sodium salt (Rb) 73–79 % fluorometric was obtained from J&K (Pforzheim, Germany). Methylcellulose (MC, Metolose SM-4000, 27.5–31.5 % of methyl groups) was kindly provided by Shinetsu Chemical Co. Dialysis membrane (Mw cut-off (MWCO): 14 kDa) was from Membra-Cel™ (Serva Electrophoresis, Heidelberg, Germany). Polyethylene glycol (PEG; 10 000 Da) and Tyramine hydrochloride (Tyr) were purchased from BIOSYNTH (Berkshire, MA, USA). 4-Dimethylaminopyridine (DMAP) 99 %, 4-Nitrophenylchloroformate 97 %, Trimethylamine (pure 7.3 M), trypsin/EDTA, Glutamine, penicillin-streptomycin, fetal bovine serum (FBS), Dulbecco's Modified Eagle Medium (DMEM) with high glucose, Hoechst, and Ethidium homodimer were purchased from Thermo Fisher Scientific (Waltham, MA, USA). Alexa Fluor 488 – Phalloidin (ab176753) was obtained from abcam, Belgium. Dichloromethane, Diethyl ether and Methanol were purchased from Chem-Lab (Zedelgem, Belgium). EA.hy926 endothelial cells were supplied by ATCC® (American Type Culture Collection).

2.2. Biomaterial modification

Methacrylated gelatin was prepared as previously described [34] based on existing reports [35,36]. The synthesis method of PEG-Tyr was performed with slight modifications of previous works [37,38] as described in the supplementary information (S1.1).

The modifications of the polymers (gelatin and PEG) were verified by ^{1}H NMR analysis using a spectrometer (JEOL JNM-ECZ600 R/S3) with D_2O as the solvent and a FTIR spectroscopy device to record ATR-FTIR interferograms (Nicolet Summit PRO, Thermo Fisher Scientific, Waltham, MA, USA) within a scan range of 4000–400 cm^{-1} and a resolution of 1 cm^{-1}. The tyramine content and the modification were monitored by UV spectrometric measurements, described in supplementary information (S1.1).

2.3. Formulation of biomaterial inks

2.3.1. Formulation of the shell ink

Several shell ink formulations were prepared based on GelMA, alginate, and MC with or without PEG-Tyr (Fig. 1, S1.2). GelMA, alginate and MC were placed in an amber glass bottle and dissolved in deionized water at 35 °C under stirring. Next, Rb and SPS were sequentially introduced to achieve 2 mM and 20 mM concentrations, respectively [39]. The mixture was stirred for 15 min before placing it in

cartridges and allowing it to cool down to room temperature before printing.

After obtaining a printable ink for the shell structure, PEG-Tyr with different concentrations (Table 1) was added to the formulation to increase the flexibility and stretchability of the biomaterial ink. Enzymatic crosslinking of the PEG-Tyr was achieved by the addition of a solution of HRP to reach a final concentration of 10 U/mL (SI, Table S1).

2.3.2. Formulation of the core ink

For the formulation of the core ink, 1 % (w/v) of gelatin was dissolved by stirring at 35 °C in 100 mM calcium chloride solution [17,40,41].

2.4. Coaxial 3D printing and hydrogel formation

The hollow scaffolds – vessels were printed using a GeSIM BioScaffolder 3.2 (Radeberg, Germany). The print head consisted of two concentric needles attached to the core and shell cartridges containing biomaterial inks. The cartridges were connected to compressed air valves that can be controlled independently and thus allow the extrusion of the core and shell inks (Fig. 1B). Before printing, the warm inks (35 °C) were placed in a UV-protected 10 mL cartridge and air bubbles were removed by ultrasonication for 30 s. The shell ink was extruded by an 800 μm diameter needle using a pressure between 70 and 75 kPa. The core ink was serving as a crosslinking slurry. For the core part, a needle of 200 μm diameter was used with a pressure of 5–8 kPa. The inks were extruded on a Petri dish, at a print head speed of 6 mm/s. Once printed, vessels were crosslinked (Fig. 1C) to obtain stable hydrogels. Photocrosslinking of the hydrogels was performed for 2 min using a visible light source (Dymax, VisiCure – 405 nm, Mavom, Kontich, Belgium). For the inks, having PEG-Tyr in their formulation, the enzymatic crosslinking was performed by spraying a 1 mM solution of H_2O_2 (approx. 300 μL) on the printed structures. The fabricated hydrogels were then immersed in distilled water to prevent them from drying out.

2.5. Characterization of the inks and hydrogels

2.5.1. Rheological behavior

The rheological characterization of the hydrogels and the biomaterial inks was performed using a plate-plate rheometer (Anton Paar MRC 302, Graz, Austria), with a 25 mm diameter plate, as described in supplementary information (S1.3).

2.5.2. Printability screening

A printability screening experiment was performed to determine an appropriate pressure range and validate extrudability and shape fidelity for inks with varied concentrations of PEG-Tyr (0–4 %) as described in the supplementary information (S1.3).

2.5.3. Swelling and degradation

The swelling and degradation of hydrogels were determined as described in the supplementary information (S1.3).

Table 1
Different hydrogel precursors - inks and hydrogel formulations, tested for fabrication of the shell part of the vessels.

Polymers used for the formulations				Hydrogel precursor - ink	Hydrogel
GelMA A % (w/v)	Alginate B % (w/v)	MC C % (w/v)	PEG-Tyr P % (w/v)		
4	3	5	**0**	PEG**0**-ink	PEG**0**-gel
4	3	5	**1**	PEG**1**-ink	PEG**1**-gel
4	3	5	**2**	PEG**2**-ink	PEG**2**-gel
4	3	5	**3**	PEG**3**-ink	PEG**3**-gel
4	3	5	**4**	PEG**4**-ink	PEG**4**-gel

2.5.4. Morphological evaluation

The visualization of the printed vessels, the channel's diameter, and their microstructure, was carried out using a light microscope (Leica DMi8 Microsystems, Wetzlar, Germany) and a scanning electron microscope (SEM) (FEI Quanta 200 FEG) [42]. The wall porosity and channel geometry were evaluated with a high-energy SkyScan 1272 micro-CT (μCT) system (Bruker Belgium SA Laboratory, Kontich, Belgium) as described in the supplementary information (S1.3). To investigate the porosity in a wet state, the vessels were prepared as described in Sections 2.3 and 2.4 with the inclusion of FITC-Dextran [43,44]. Then, using the confocal microscope (ZEISS LSM 900, 5× objective lens), z-stack images were taken to visualize the vessels in their wet state [43].

2.5.5. Compressive and tensile strength measurements

Mechanical properties of gel and PEG-gels were evaluated with a mechanical testing machine (Shimadzu AGS, Hertogenbosch, The Netherlands) with a load cell of 20 N.

The compressive and elastic moduli were obtained from the slope of the linear region of the stress-strain curves. To evaluate the elongation of the hydrogel, measurements of hydrogel length were taken before and after stretching. The integration value of the area under the stress-strain curve was reported as hydrogel toughness [45]. Details are provided in the supplementary information (S1.3).

2.5.6. Endothelial EA.hy926 cells and hydrogel seeding

The EA.hy926 transformed cell line was used to investigate the properties of our hydrogel-material *in vitro* as it was previously demonstrated to preserve the properties of the primary Human Umbilical Vein Endothelial Cells (HUVECs) [46]. To evaluate hydrogel biocompatibility and ability to serve as a support for cell growth and proliferation, ECs were seeded on the material and cultured for 1–7 days to examine cell behavior as described in the supplementary information (S1.3).

2.5.7. Cell viability and cytoskeleton staining

Cell viability over time (1, 3 and 7 days) was assessed using the MTS assay (CellTiter 96® Aqueous One Solution Cell Proliferation Assay, Promega, Madison, WI, USA). The distribution of Live/Dead cells on hydrogel specimens after 24, 48 and 120 h was evaluated by incubating cells at 37 °C for 45 min with 10 μg/mL Hoechst and 10 μM Ethidium homodimer diluted in DPBS. Cytoskeleton staining was performed with 10 μg/mL Hoechst and 2 μM Alexa Fluor 488 – Phalloidin in DPBS, with 1 % BSA. Details of MTS assay, Live/Dead and cytoskeleton staining are described in supplementary information (S1.3).

Cell morphology and adhesion were examined by SEM (as described in the SEM section) in cell-seeded scaffolds fixed by 2.5 % glutaraldehyde solution, and subsequently dehydrated with graded ethanol series (50, 75, 90 and 98 %) before air-drying for 3 days and metal-coating.

2.5.8. Chorioallantoic membrane (CAM) assay

The CAM assay was used to investigate hydrogel material biocompatibility and angiogenic properties according to a previously described method, with slight modifications [47–49], as described in the supplementary information (S1.3). We performed a quantitative analysis of the vessel area, total vessel length and number of branching points for the specified area (rectangle marked in Fig. 7F, G, H) from each taken photograph [49].

2.5.9. In vivo studies - sub-fascia implantation rat model and hydrogel testing

Adult female Wistar rats (250–300 g) were used in the sub-fascia implantation model experiments. On the subfascial plain above the spinotrapezius muscle on each animal's dorsum, two pockets were created in order to implant the hydrogel (on the left side) and the glass fiber as the negative control (on the right side). Implanted materials and

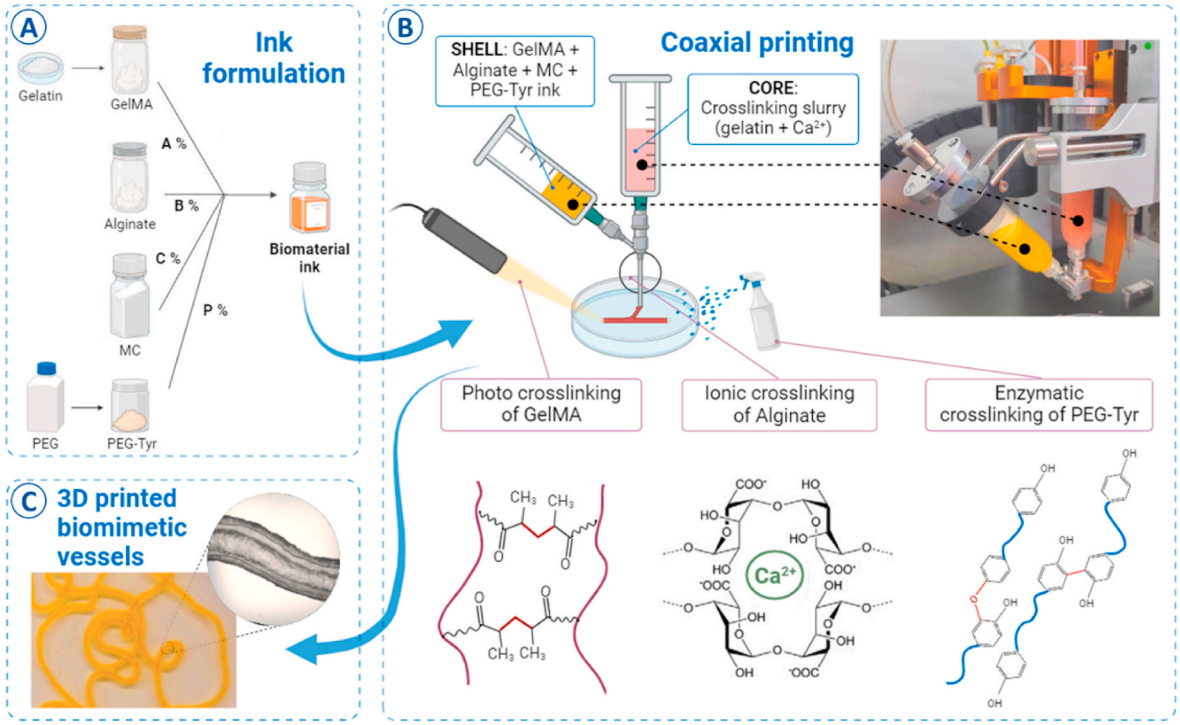

Fig. 1. A) Formulation of the shell ink; B) Schematic of the coaxial printing setup assisted by a multifaceted crosslinking procedure (combination of ionic and enzymatic crosslinking with photocuring) with photo of the core-shell system of Bio Scaffolder used for vessel 3D printing; C) 3D printed vessels.

surrounding tissue were explanted for histological analysis at different time points.

Histological samples were marked with hematoxylin and eosin (HE) staining to identify the general features of the host tissue reaction. The number of blood vessels per mm^2 was counted in four random fields per slide in both the hydrogel implantation site and in the surrounding tissue (perilesional). The photomicrographs were analyzed using NDP view software. The counted lumens containing red blood cells were highlighted on the histological images (red circles in the lesion and green circles perilesional). The microvessels' densities were calculated as vessels/mm^2. We also evaluated the levels of IL-8 in rats' blood to check for inflammation. All histology images are included in the supplementary files (S1.3). All the experimental procedures were approved by the Ethical Committee of Grigore T. Popa University of Medicine and Pharmacy of Iasi (registration no. 83/May 25, 2021) and are described in detail in the supplementary information (S1.3).

2.5.10. Perfusability evaluation

The perfusability of the vessels was evaluated using an in-house built polydimethylsiloxane (PDMS) microfluidic chamber under steady-state flow with a syringe pump (Perfusor® fm B|Braun), or a pressure controller (Microfluidic Flow Control System – Fluigent, Jena, Germany) and set of channels and Luer-lock connectors. A solution containing distilled water and blue or red food coloring was perfused through the vessel under microscopic observation. Flow rate ranged from 0.1 mL/min, up to approx. 5 mL/min, to mimic blood flow in veins below 800 μm [50]. For the burst pressure experiment, we initially set the pressure on the pressure controller and monitored it directly from the device. The set pressure was then systematically increased, until the tube eventually ruptured. At each pressure increase interval, the system was allowed to stabilize for approximately 10 s. To observe bursting, one end of the tube was sealed, leading to a gradual pressure buildup in the channel until failure [51]. Details are provided in the supplementary information (S1.3).

2.6. Statistical analysis

All data are presented as the mean ± standard deviation, on a minimum of three independent measurement replicates. Statistical analyses were performed using a one-way ANOVA with a Tukey post hoc test. Differences between groups were reported as significant at $p < 0.05$. The letters used on a bar chart (a, b, c) represent statistical significance between the groups. Bars with different letters are statistically different from each other at the significance level ($p < 0.05$).

3. Results and discussion

3.1. Rational design of hydrogel

3.1.1. Biomaterial modification and chemical characterization

A phenol-functionalized polyethylene glycol was synthesized in a two-step reaction by conjugating Tyr to the PEG backbone (Fig. 2A). First, an amine-reactive PEG (PNC-PEG-PNC) was synthesized using PNC molecules. The ^{1}H NMR spectra of PNC-PEG-PNC showed two new peaks at 6.9 and 8.0 ppm, corresponding to the aromatic protons of PNC, distinct from the PEG spectra. This confirmed the conjugation of PNC to the PEG backbone [38]. In the second step, PEG-Tyr was synthesized through the formation of a urethane bond between Tyr and PNC. The ^{1}H NMR spectroscopy of PEG-Tyr showed a doublet at 6.9 and 7.2 ppm, which corresponds to the aromatic proton of tyramine [37,38]. This observation confirmed the successful modification of PEG. The tyramine content was recorded by UV spectrometric measurement (Fig. 2B) and quantified based on the calibration curve (Fig. 2C). The PEG-Tyr sample contained 83.7 μmol of tyramine per gram of PEG-Tyr. This value is consistent with previous studies, reporting phenol content of 98–200 μmol/g [32].

The chemical structure of PEG-PNC and PEG-Tyr was also characterized using FTIR spectroscopy (SI, Figure S1). The FTIR spectrum of PEG-PNC shows a peak at 1648 cm^{-1} and 1561 cm^{-1}, which indicates the $–NO_2$ group of PNC, confirming the presence of PNC molecules on PEG backbone [52]. Both the PEG-PNC and PEG-Tyr spectra show the

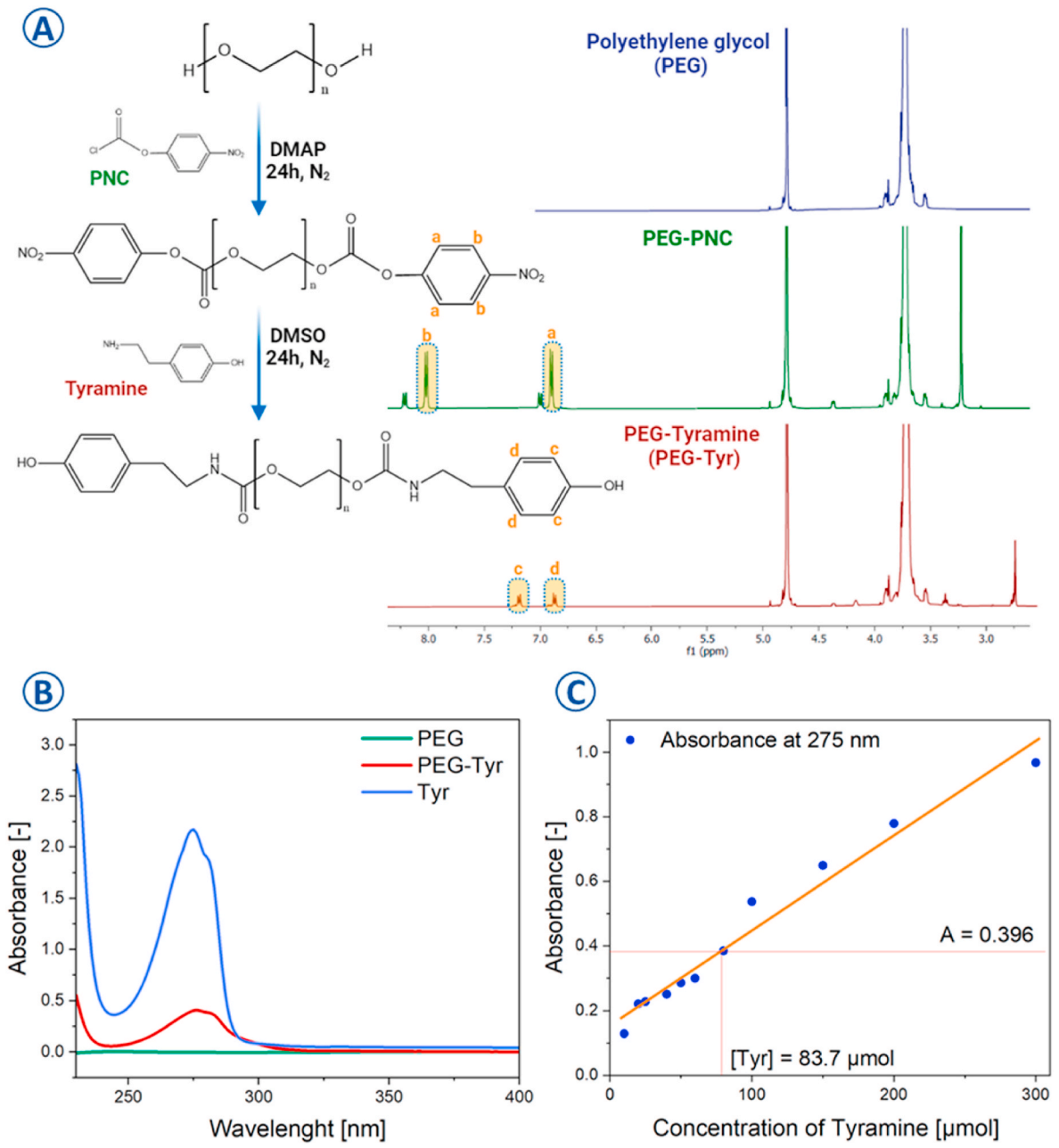

Fig. 2. A) NMR Spectrum of PEG, PEG-PNC, PEG-Tyr, with synthesis route on the lefthand side; B) UV–visible spectroscopy of PEG, PEG-Tyr, Tyr; C) Calibration curve plotting the relation between absorbance and concentration of Tyr.

characteristic peaks of PEG, including the absorption band at 2884 cm^{-1} corresponding to the aliphatic C–H stretching band and peaks at 1466 and 1341 cm^{-1} corresponding to C–H bending vibrations. The IR bands at 1279 and 1095 cm^{-1} demonstrate the stretching of the O–H and C–O–H bonds [53,54]. The peak at 1095 cm^{-1} has a lower intensity for PEG-PNC and PEG-Tyr, likely due to the partial substitution of the O–H in PEG by molecules of PNC and tyramine. Additionally, peaks typical for amines (–NH stretching) at 3380–3280 cm^{-1} are absent in PEG-Tyr, which shows that the tyramine is bonded via PNC to the modified PEG backbone [55]. The successful conjugation of PEG with Tyr was also demonstrated through the formation of a hydrogel upon enzyme-mediated crosslinking (SI, Table S1) [38]. The ^{1}H NMR for modified gelatin has proven the presence of methacryloyl groups, in agreement with the literature [35]. The methacrylation degree of gelatin was estimated at 56 %, as we reported previously [34]. The degree of GelMA functionalization close to 50 % was previously reported to result in softer properties, which is more favorable for promoting vascular formation, compared with GelMA containing approx. 75 % of methacryloyl units [18].

3.1.2. *Multifaceted crosslinking*

Ionic crosslinking at the interface of the shell and core material was employed during the coaxial extrusion. Ca^{2+} ions were introduced to the gelatin core, so that adjacent alginate chains with carboxyl groups formed ionic bonds with Ca^{2+}, following the “egg box model” [56]. Photocrosslinking further stabilized the vessel structures after printing, leveraging methacrylamide and methacrylate side groups in GelMA’s chain. These groups formed covalent bonds upon visible light exposure using a photoinitiating system (Rb/SPS) [36,39]. In the final stage, enzyme-mediated crosslinking induced covalent bonds in PEG-Tyr chains.

PEG-Tyramine contains tyramine functional groups that are

susceptible to oxidation. In the presence of an oxidizing agent, HRP, and H_2O_2 as the initiator, the tyramine moieties undergo oxidative reactions [39]. HRP catalyzes the conversion of tyramine to highly reactive o-quinone intermediates, which undergo C–C and C–O covalent bond formation with neighboring tyramine residues or other nucleophilic groups in the hydrogel matrix [37,57].

In this study, hydrogel precursors (polymeric blends) are referred to as "inks" and after crosslinking materials are referred to as "hydrogels".

3.2. Rheological characterization of the inks and hydrogels

The viscoelastic properties of the inks and the hydrogels were evaluated prior to printing (Fig. 3). All tested materials showed the properties of solid viscoelastic materials as observed by higher G′ than G'' (Fig. 3C and D) [58,59]. The inks showed shear-thinning and frequency-dependent behaviors which are suitable for extrusion 3D printing as observed in flow curve and frequency sweep results (Fig. 3A–E) [41]. Concerning the effect of PEG-Tyr on the rheological properties of the ink and hydrogel, the viscosity, G′ and G'' of the ink formulation decreased by increasing PEG-Tyr concentration from 0 to 4 % (Fig. 3A, and SI, S.2 A), which was not observed upon crosslinking (Fig. 3B and F and SI, S.2 B). The decrease in viscosity can be attributed to the presence of PEG (10 kDa), acting as a plasticizer, owing to its low viscosity and molecular weight [60–62]. However, the use of higher molecular weight (20 kDa) PEG has been reported to have a negligible impact on the material's viscosity [13,37]. PEG chains are known for their ability to form flexible and hydrophilic structures. In the ink formulations that include PEG-Tyr, the PEG chains act as a spatial barrier

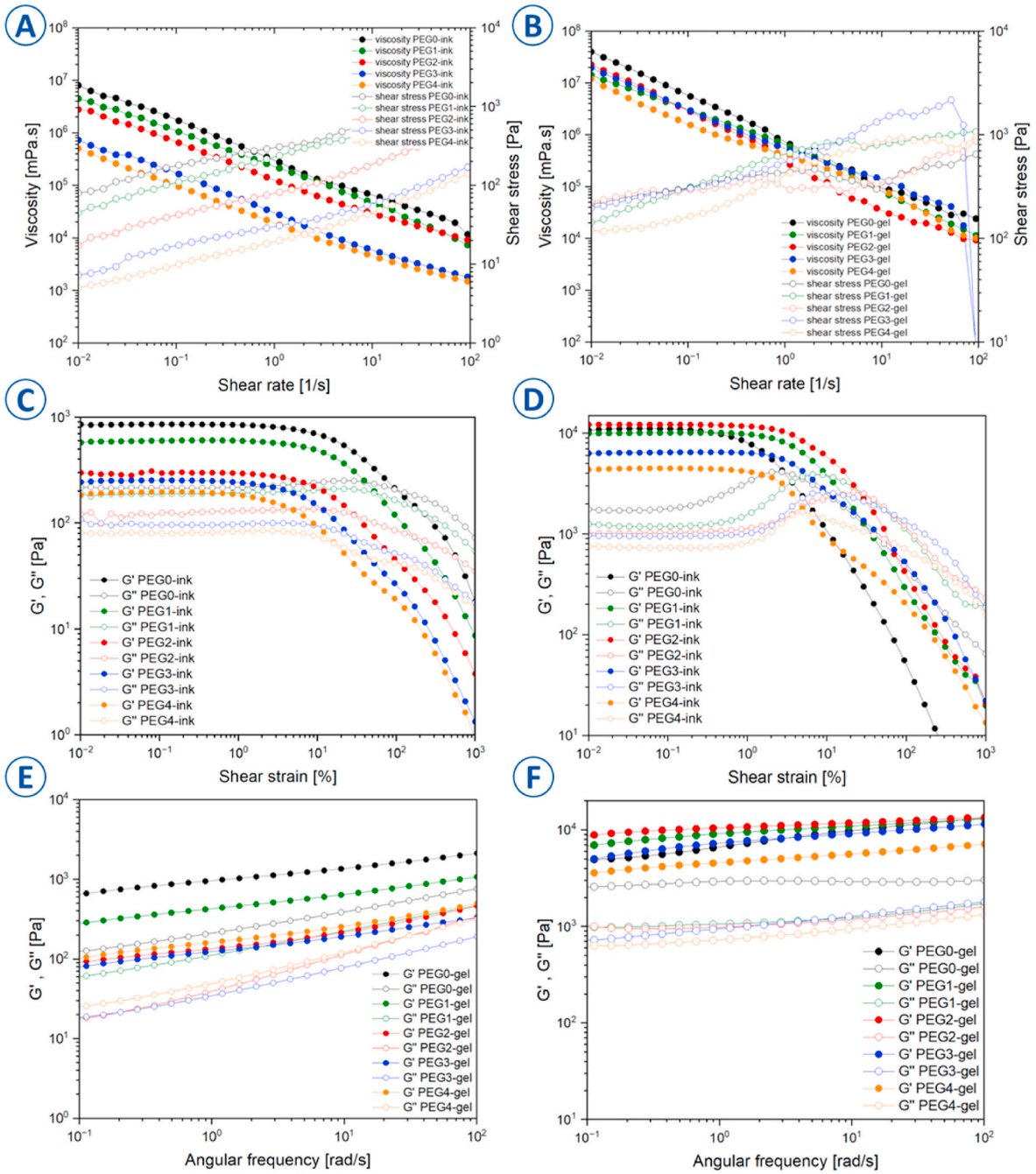

Fig. 3. Viscosity and shear stress of A) inks B) hydrogels; Amplitude sweep C) inks formulations and D) hydrogels; Frequency sweep for E) inks and F) hydrogels. Representative plots from three independent measurements were shown.

between the polymer chains of GelMA, alginate and MC. This spatial separation enhances the molecular mobility within the ink, resulting in a decrease in viscosity [60,61]. The presence of PEG-Tyr facilitates the movement of polymeric chains leading to a decrease in both viscosity and elasticity [60–62]. With increasing PEG-Tyr concentration from 0 to 4 %, there was a notable difference in the gap between storage and loss moduli of the inks in LVR, decreasing from 650 Pa to 115 Pa [63], resulting in a liquid-like system and therefore, poor printability (Fig. 3C). With increasing PEG-Tyr concentration (0–4 %), the flow point also shifted to lower shear strain values (from 100 to 10 %), implying that less pressure is required for the ink to flow in the nozzle during extrusion printing [63]. The addition of PEG-Tyr, up to 2 % (w/v) increased the loss tangent value (SI, Figure S2C). The loss factor, represented by the loss tangent, is an indicator of the material's ability to absorb and dissipate energy in response to deformation [64], and it reached the highest value of 0.4 at a PEG content of 2 %. This indicates the superior formability and flexibility of the PEG2-ink, compared to the PEG0-ink (with a loss factor of 0.25). After crosslinking, in both amplitude and frequency tests (Fig. 3D–F), all hydrogels showed a nearly 10-fold increase in the values of G′ and G″, demonstrating the stabilization of the hydrogel systems. The crosslinking density values were below 0.4 mol/m^3 for the inks and above 2.1 mol/m^3 for the hydrogels, indicating the successful crosslinking process (SI, Figure S2 D) [63]. The highest density of the formed crosslinks was observed for PEG2-gel (4.1 ± 0.3 mol/m^3), due to the enzymatic crosslinking of PEG-Tyr which strengthened the network, especially when the PEG-Tyr concentration remained below 3 %. Achieving an optimal extrusion printing requires a balance between the concentration of the PEG-Tyr and the associated material properties. Based on the rheological evaluation, we have determined that the ideal concentration range for PEG-Tyr lies between 1 and 2 %.

3.3. Hydrogels' mechanical properties

In addition to rheological behavior, the presence of PEG-Tyr in the hydrogel formulation significantly influenced the mechanical properties and elasticity of hydrogels (Table 2, Fig. 4). To mimic blood vessels, the hydrogels must have similar strength and elasticity [65] to withstand blood pressure. The compressive modulus of hydrogels with PEG-Tyr was lower than ~8 kPa, compared to the reference – PEG0-gel (~15 kPa), demonstrating that PEG-Tyr softens the hydrogel structure and decreases material stiffness, bringing material properties closer to native small blood vessels (Young modulus below 10 kPa) [65]. The addition of PEG-Tyr creates extra interactions between polymeric networks, improving the overall performance and robustness of the hydrogels. PEG-based hydrogels have previously proven their ability to tune material stiffness [27]. Hydrogels reported in this study are in the same order of magnitude as reported previously by Qingmeng et al. (13 kPa) for composite GelMA, alginate, modified PEG [66] and PEG-based hydrogels [67], which have proven good performance in tissue engineering applications. Additionally, bulk hydrogels with a modulus lower than 20 kPa were shown to get more efficiently colonized by cells exhibiting less rounded morphology [68], which agrees with our observations during cell culture (Fig. 8E and F). Recently, Leonard-Duke et al., showed that PEG-based hydrogels with stiffness below 20 kPa can facilitate HUVECs sprouting, in terms of their number and length

Table 2
Mechanical test data, based on tensile measurements.

Hydrogel formulation	Elongation at break [%]	Tensile strength [kPa]
PEG0-gel	37.8 ± 2.8	20.3 ± 3.3
PEG1-gel	52.5 ± 3.3	21.2 ± 0.8
PEG2-gel	63.1 ± 3.9	18.4 ± 3.4
PEG3-gel	84.6 ± 2.7	22.9 ± 2.1
PEG4-gel	108.3 ± 4.0	26.4 ± 2.1

Table 3
Mechanical test data, based on compression measurements.

Hydrogel formulation	Compressive Modulus [kPa]	Compressive strength [kPa]	Toughness [J/m^3]
PEG0-gel	14.9 ± 0.1	9.0 ± 0.9	4.6 ± 0.9
PEG1-gel	3.5 ± 0.8	>5.3 ± 1.0	5.9 ± 0.7
PEG2-gel	7.6 ± 0.1	>21.5 ± 3.2	5.3 ± 1.3
PEG3-gel	6.3 ± 0.3	4.3 ± 0.9	2.0 ± 0.1
PEG4-gel	7.4 ± 0.6	14.5 ± 1.1	14.4 ± 2.1

[69]. The influence of the PEG content on the mechanical properties of the hyaluronic acid-PEG hydrogel was investigated previously [37]. It was found that the higher the concentration of PEG is, the more hydrogel can be compressed without permanent deformation. We observed a similar relation in our study as hydrogels without PEG could be compressed up to 30 % while adding 1–2 % of PEG-Tyr material was compressed without fracture propagation to more than 55 % of its initial height (Fig. 4A–D). This proved that the addition of PEG led to the formation of hydrogel with boosted elastic properties [37]. Increased gel stiffness can translate for lower cell adhesion, migration, and vessel sprouting [69], leading to reduced permeability and increasing cell mortality [69]. The addition of PEG (up to 3 % w/v) also resulted in less-tough hydrogels 2–6 J/m^3) (Table 2), which may provide a favorable environment for cell infiltration [70]. The presence of plasticizing PEG and MC, which had not undergone cross-linking, can be the explanation for the relatively low toughness of our hydrogels [71] (see Table 3).

Lack of sufficient elasticity in small-diameter vessels leads to small subcutaneous effusions when vessel breaks, but also promotes cellular-level dysfunction in the vessel wall [72]. Hence the current design of artificial vessels should address this issue. The linear structure of PEG chains allows them to slide over one another, and elongate when subjected to stress [73]. Concerning our hydrogels, when PEG-Tyr content increased from 0 to 4 %, stretchability (elongation at break) increased from about 40 to 110% (Fig. 4B and C). The phenomenon of necking deformation of the material was noted, while stretched to a certain point, which is not observed in brittle materials like pure GelMA hydrogel [16,74]. This suggests that the existence of crosslinked PEG-Tyr enhanced the networks and strengthened the entire system. The flexibility of PEG-enriched hydrogels, understood as enhanced elasticity, is mainly attributed to PEGs' linear polymer chain and the lack of steric hindrance [73]. PEG-Tyr crosslinks (Fig. 4E) translate for the flexibility and stretchability of the material, despite the similar tensile strength (~20 kPa) noted for all hydrogels [73].

3.4. Morphological properties of the vessels

Morphological analysis was performed for vessels made of PEG2-gel which demonstrated favorable printability and mechanical properties. The μCT and SEM measurements provided the presence of a hollow inner channel within the constructs, confirming the successful fabrication of vessel-like structures (Fig. 5A–E). Fig. 5A–G revealed the uniform porous structure of the hydrogel in a dry state. (Fig. 5F).

To characterize the structural properties of the vessels in a wet state, we visualized freshly printed vessels containing FITC-labelled dextran macromolecules with a confocal microscope. The wet hydrogel shows a porous structure (Figure S9, SI), with smaller surface pores (Figure S9A, SI) and larger pores in the intrinsic layers (Figure S9 B-D, SI) [75], demonstrating the pore-forming capacity of our hydrogels [43,44]. Diffusional permeability of the hydrogel vessel may be seen in Fig. 6H in 4–6 s of perfusion. Permeability in a wet state is crucial for the infiltration of cells, provision of nutrients and metabolite transportation [76,77]. The vessel structure in the wet state owes its permeability mainly to the MC component, interlocked by the cross-linked polymers, however, gradually leaching out in the hydrophilic environment. Confirmation of

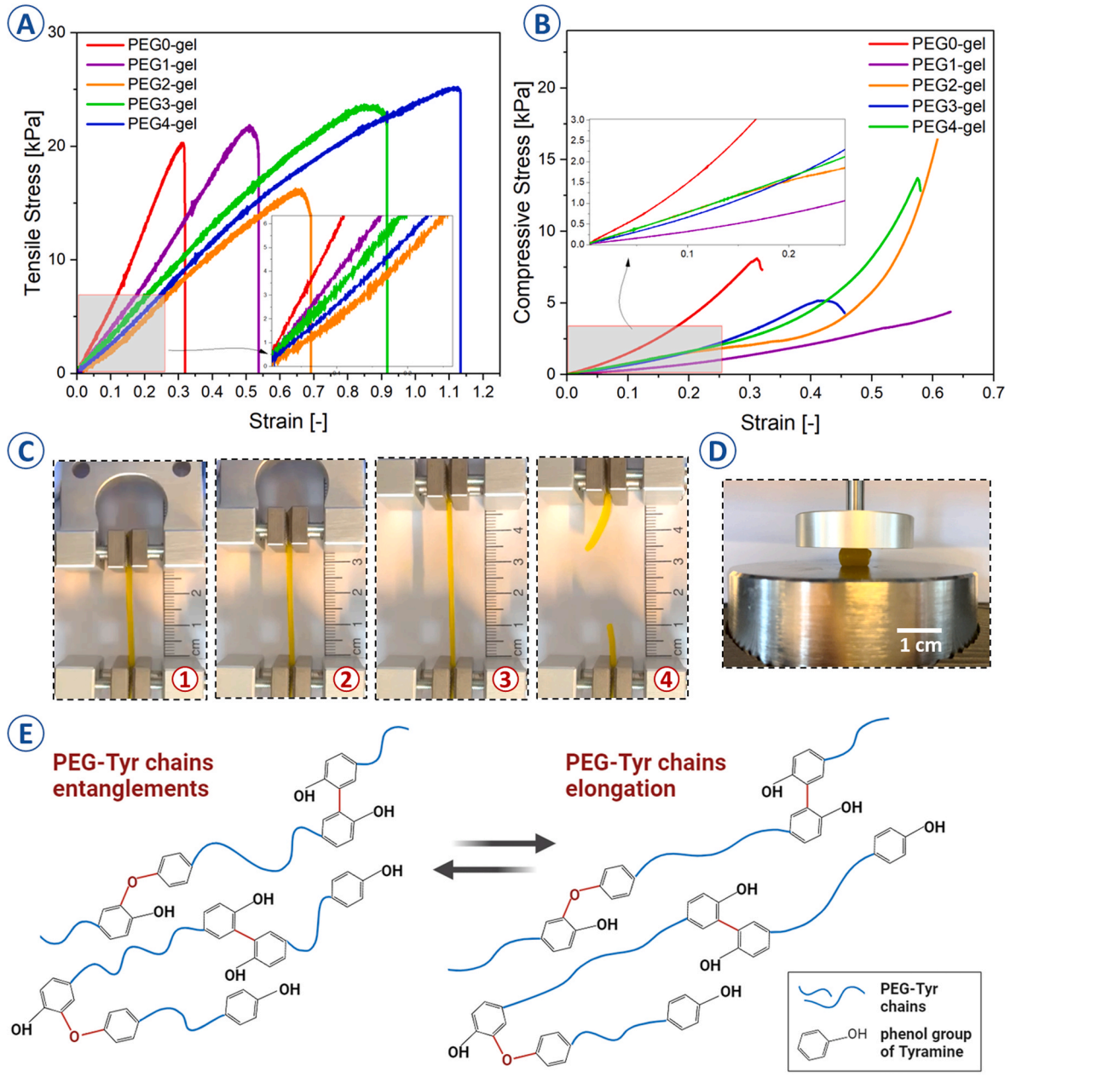

Fig. 4. Representative stress versus strain curves for different hydrogels (with and without PEG, n = 3) A) tensile test and B) compressive test; Images taken during the mechanical test of the PEG4-gel are shown in C) for tensile test and D) for compression; E) Graphical representation of the elongation of PEG-Tyr chains in response to the tensile force.

this observation can be seen in Fig. 8D, where cells infiltrate a loosening polymer network and fill the voids of the vessel wall [44]. Structures with porosity and sponge-like architectures may allow ECs with a size between 14 and 15 μm to travel through the voids and attach to the GelMA chains with the help of RGD adhesion sequences [78,79].

3.5. Swelling and degradation mechanisms of the hydrogels

The swelling capabilities of hydrogels help to mimic the native environment of tissues [80] and in addition to mechanics and rheology, provide insights into material stability in aqueous media. Hydrogels in this study absorbed most of the media (PBS) within the first 8 h of immersion at 37 °C (Fig. 5H). Swelling was equal to 850 ± 8.7 % for gel, and about 1.25 times lower for PEG1-gel (697.1 ± 4.6 %) and PEG2-gel (671.6 ± 8.6 %). Lower capability to absorb media can be attributed to an increase in crosslinking density resulting from PEG-Tyr presence as determined by inks and hydrogels rheological studies (SI, Figure S2 D). Despite the high ability of the hydrogels to swell, the perfusion channel is preserved and functional (SI, Figure S5 A, B) and inner tube diameter only slightly decreases (SI, Figure S5C, D). Generally, the higher the crosslinking density, the lower the swelling ratio [81]. However, as shown in rheological investigations, by further increasing PEG-Tyr concentration to 3 or 4 % G′ and G″ decreased and the hydrogels degraded faster. These hydrogels absorbed nearly double the amount of media, compared to gels with 1 or 2 % of PEG-Tyr. The structural weakening observed when PEG content exceeds 2 % may be explained by the fact that PEG acts as a plasticizer, neutralizing the effects of other cross-linking pathways [61,62]. PEG-Tyramine can enhance the hydrogel's swelling behavior due to the hydrophilic nature of PEG moieties [32,33]. PEG has water-absorbing capabilities and imparts high

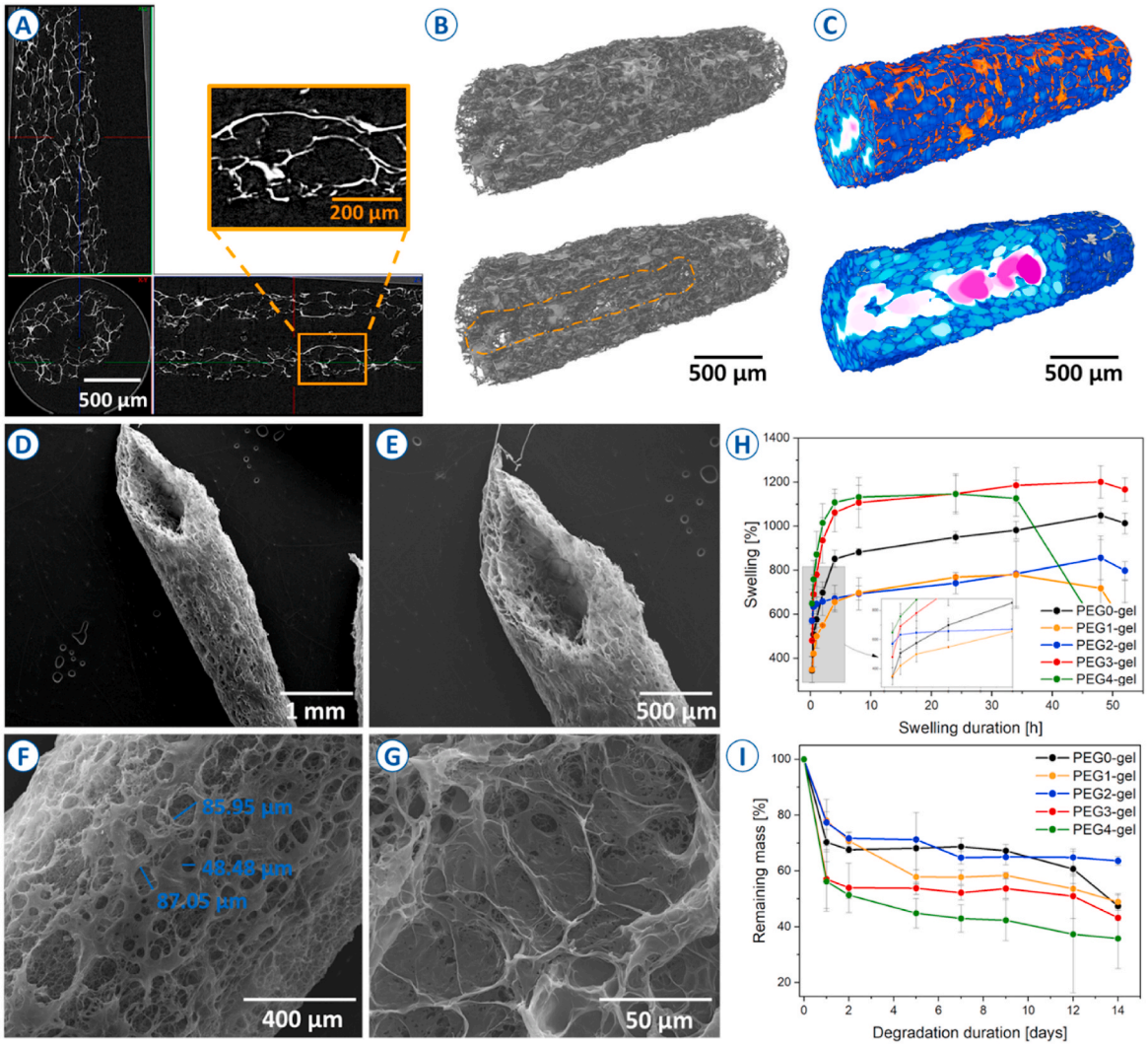

Fig. 5. A) µCT scan showing a porous structure of the PEG2-gel vessel and an empty channel in the vessel interior; B) and C) show the reconstructed 3-dimensional PEG2-gel vessel structure with analysis of thickness and separation in vessel interior and exterior; D-G) SEM images of printed PEG2-gel hydrogels; H) Swelling test for hydrogels with varying PEG concentration; I) Degradation behavior of hydrogels with varying PEG concentration, n = 3.

hydrophilicity to the hydrogel. Additionally, tyramine groups can undergo oxidative coupling reactions, forming covalent bonds upon exposure to enzymatic or chemical stimuli [82]. This crosslinking can influence the hydrogel's network structure, providing stability while allowing for water absorption and swelling. The extent of swelling may be modulated by the concentration of PEG-Tyramine and the degree of crosslinking achieved during gelation.

Concerning the hydrogel degradation processes (Fig. 5I), the mass loss during the first days can be related to the dissolution of non-crosslinked MC, leaching and softening the structure prior to covalent bonds degradation [71]. PEG1-gel and PEG2-gel lost ~30 % of their mass in the first two days, while hydrogels with higher amounts of PEG (3 and 4 %) lost ~50 % of their mass in the same period. PEG is not easily degradable in a cellular environment, however, when it is blended with other biodegradable polymers such as gelatin or alginate, its network begins to disintegrate [83]. As previously shown, PEG-gel degrades within 6 weeks when blended with hyaluronic acid [37].

As shown in the µCT scan (Fig. 5A) and wet-sate fluorescent images (Figs. S9 and SI) vessel walls' are similar to that of fenestrated or sinusoidal capillaries [3]. A reduction of about 50 % of the hydrogels' original mass was noted after two days but did not change significantly over the following two weeks (Fig. 5I). This may be due to the drawn-out process of breaking strong covalent bonds, not cleaved during the first days of immersion [84]. During the test, samples retained their original shape and did not fragment, proving the gradual dissolution of polymers. Such progressive degradation allows for gradual infiltration of the cells. In the context of vascular tissue engineering, thanks to the degradation mechanisms, a protective outer layer of the basement membrane can gradually form as the hydrogel scaffoldings get substituted with ECs and pericytes [85].

3.6. *Core-shell printing of vessels*

Utilizing core-shell 3D printing and multifaceted crosslinking, we 3D-printed vessels with uniform wall thickness and shape stability (Fig. 6D–F). According to the 3D printability test, the formulation with 4 % GelMA, 3 % alginate and 5 % MC was selected as the reference ink – PEG0-ink (SI, Section S1.2.). This ink had a suitable viscosity to maintain the structure during printing [86] and to avoid nozzle clogging or creating breaks in the printed pattern [87,88].

To enhance the flexibility and stretchability of the printed vessels [13,37], 1–4 % of PEG-Tyr was added to the formulations and denoted as "PEG1-ink" to "PEG4-ink. Printability screening was carried out to first verify the impact of PEG-Tyramine on material printability (SI, Figure S3 A-E) and later establish suitable pressure conditions to print vessels (SI, Figure S4 A-C). PEG2-ink had good flow properties and

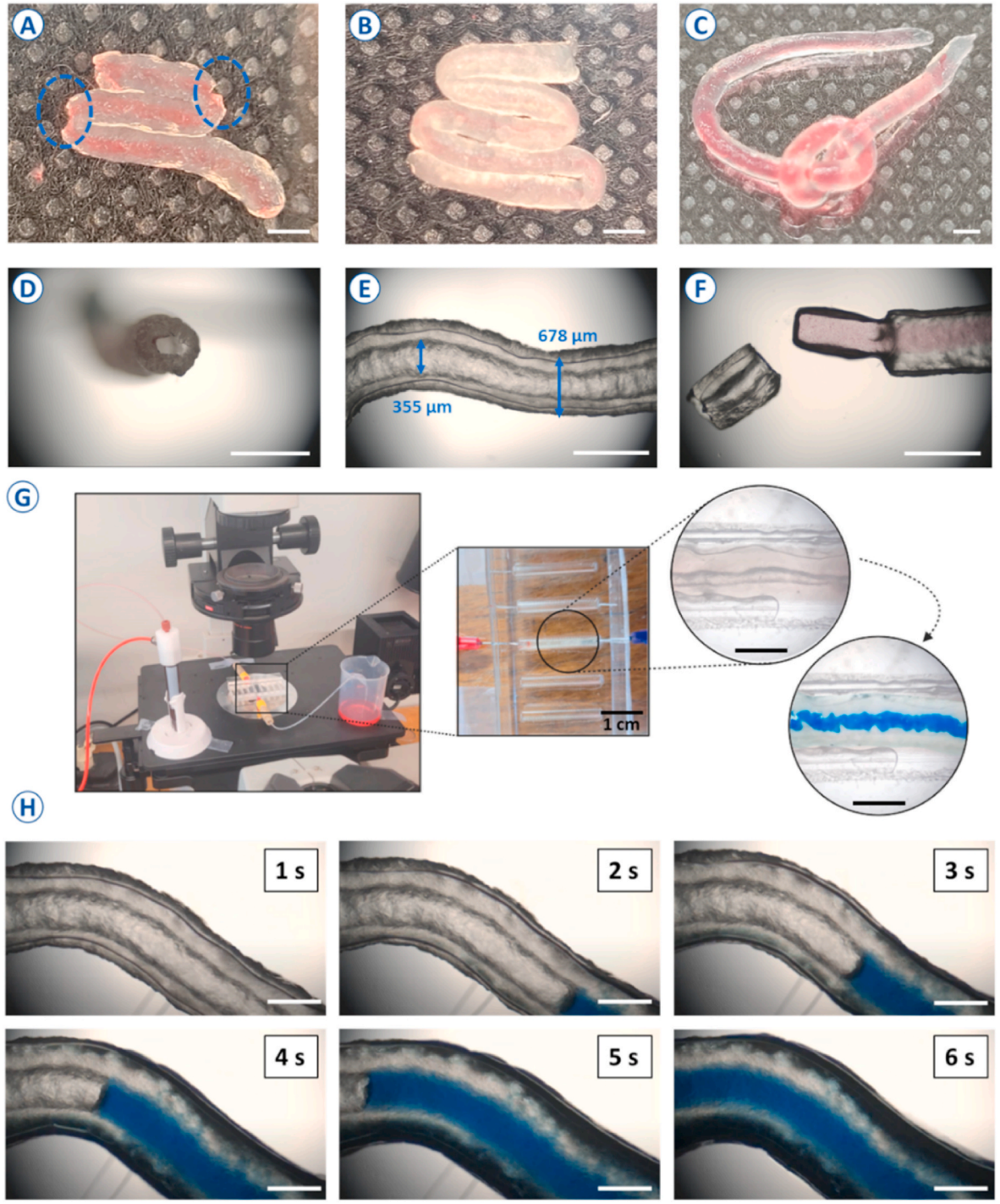

Fig. 6. Evaluation of the vessels flexibility; A) Bending of the gel vessel; B) Bending and C) knotting of the PEG2-gel vessel; Optical microscope images of a printed vessel placed: D) vertically (showing the cross-section); E) horizontally (showing dimensions of hollow channel); F) printed vessel before removing the core part; G) In-house-made setup for perfusion tests, showing the PDMS chamber with channels and vessel fixed and perfused during experiments; H) Perfusion test carried out for the PEG2-gel vessel, under the optical microscope. Scale bar corresponds to 1 mm unless stated otherwise.

strength after crosslinking (PEG2-gel), giving the printed vessels the desired flexibility. PEG3-ink and PEG4-ink were spreading uncontrollably even at low pressures disqualifying them from forming structures with lumen (SI, Figure S3 D, E). We therefore 3D printed the vessel's shell layer using the PEG0-ink and PEG2-ink (Fig. 6A and B).

The gelatin and Ca^{2+} ions in the core ink can be easily removed from the inner part of the tube by placing in warm water or culture media (~30 °C) [89]. Fig. 6F shows a printed tube before removing the core part, which is distinguished by red food coloring [17,40,41].

Endothelial cells are mechano-sensitive to vessel stiffening [90], and an ideal hydrogel mimicking natural vessels must be biocompatible with good cell adhesion and offer flexibility and stretchability [91,92]. Crosslinking also affects the spacing and arrangement of polymer chains, influencing the overall porosity of the hydrogel. The degree of crosslinking and its impact on porosity can be controlled by adjusting the concentrations of PEG-Tyr, Alg, and GelMA. Alginate contributes to ion-mediated crosslinking, methylcellulose influences viscosity and gelation [93], and gelatin might enhance cell adhesion and bioactivity

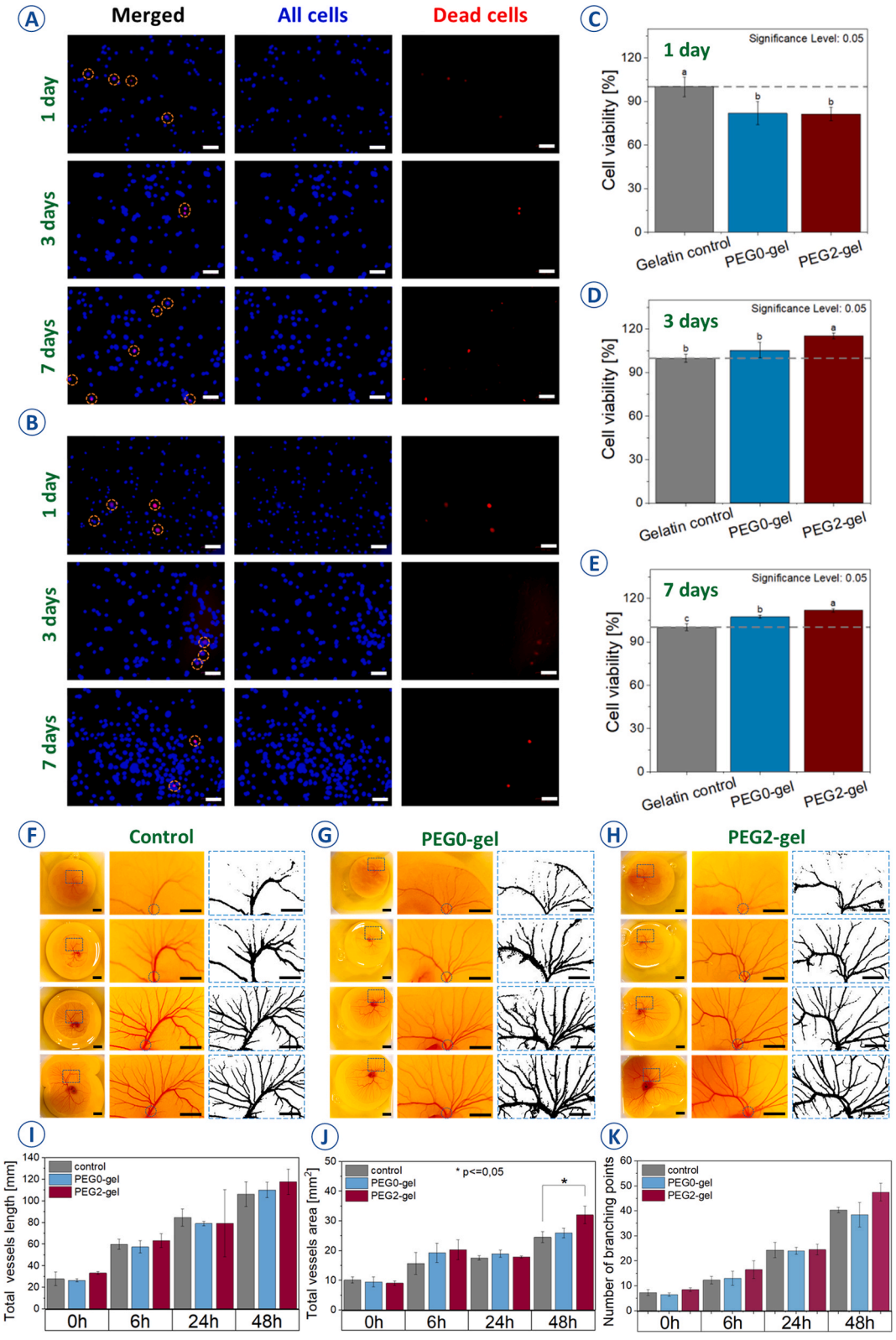

Fig. 7. A) Live/Dead staining of EA.hy926 cells cultured on A) PEG0-gel and B) PEG2-gel, scale bars correspond to 100 μm; Cell viability results after C) 1 day, D) 3 days and E) 7 days for cells cultured on PEG0-gel, PEG2-gel, gelatin layer (used as an experiment control-100 % viability indicated by the dashed line), n = 3; Photographs of the different stages of CAM development (n = 3) at 0 h, 6 h, 24 h and 48 h, where: F) control, G) samples with the PEG0-gel and H) samples with the PEG2-gel. The first column shows the entire CAM area, the second column shows the area where the material was placed and used as a region of interest (ROI) for the quantitative evaluation, and the third column is a binary version of the ROI used for the evaluation of the formed blood vessel network, scale bars correspond to 10 mm. Based on the images analysis, I) the total vessel length, J) the total vessel area and K) the number of branching points, calculated at different experimental time points.

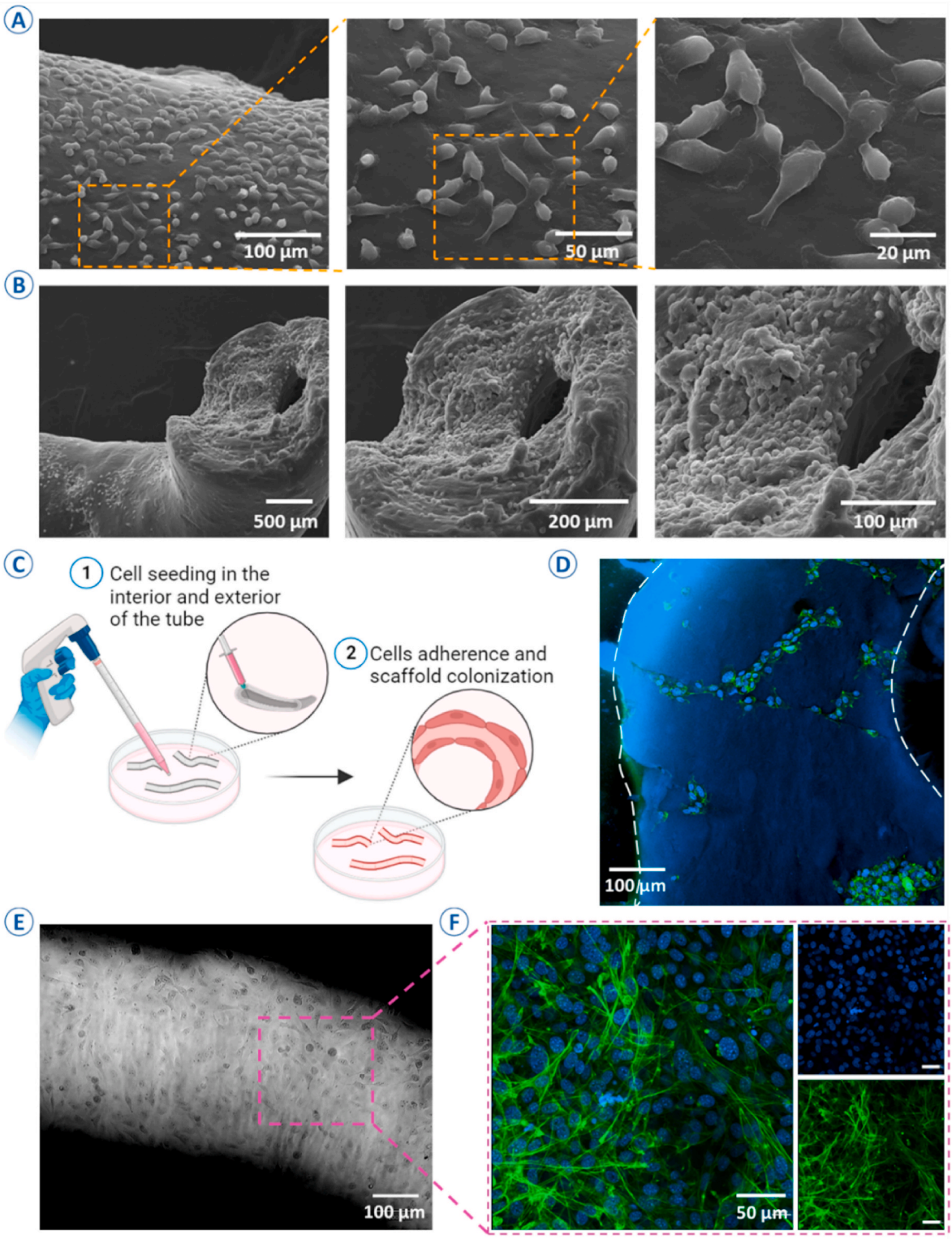

Fig. 8. SEM images of 3D-printed, vessels showing A) cells adherence to the surface of PEG2-gel, B) cells located concentrically around the vessel inlet; C) Schematic representation of cell seeding in the interior and exterior of the vessels; D) Confocal image of vessel cross-section revealing cells infiltrating voids in vessel wall; E) Bright-field image of cells adjacent to the vessel scaffold; F) Confocal images showing cells adhering to the vessel, with cytoskeleton stained in green and nuclei in blue.

[34].

We examined the vessels' flexibility and elasticity through basic bending and knotting. PEG2-gel vessels withstood bending (Fig. 6B) and knotting (Fig. 6C), due to the elasticity introduced by the addition of PEG. However, the vessels printed with PEG0-ink were not flexible and fractured upon bending (Fig. 6A). This rigidity can be due to the rapid cross-linking of alginate, leading to the formation of a brittle and stiff material [94]. Coaxial printing added flexibility to the structures and significantly decreased the channel size compared to the dimensions achievable in conventional extrusion printing (from about 4 mm to

300–400 μm) [95]. This made the printed geometry closer to its natural form [95]. PEG0-gel-vessels' had an outer diameter of 660 ± 14.4 μm, an inner diameter of 320 ± 5.9 μm and an average wall thickness of 168 ± 19.4 μm. The 2 % PEG-Tyr had no significant impact on the dimensions. We succeeded in fabricating vessels with diameters smaller than previously reported for coaxial printing (630–1300 μm) without impairing critical structural integrity [96].

We aimed to mimic the morphological features of sinusoidal and fenestrated capillaries. This approach involves creating a single porous layer, serving as a means for structural prevascularization in tissue-engineered scaffolds to enhance scaffold vascularization *in vitro*. Examinations of cross-sectioned tubes revealed a uniform wall thickness (Fig. 6D), and an adjustable lumen size through process variables such as the nozzle diameter, printing speed, viscosity and degree of crosslinking [97]. Microscopic images revealed a uniform vessel wall (Fig. 6E). The tubes possessed sufficient rigidity to maintain their shape without collapsing due to gravity, thus retaining their initial geometry [16]. As such, coaxial 3D printing may be used to replicate arterioles and venules apart from large-diameter vascular structures [98,99].

3.7. Vessel's perfusion and burst

Vessels printed through coaxial methods can be perfused with fluids (Fig. 6G), facilitating cell growth and multiplication. Pressure fluctuations from 14 to 71 mmHg and from 11 to 52 mmHg can be noted in the arterial and venous parts of skin capillaries, respectively [72]. We successfully perfused our vessels with a defined pressure ranging from 18 to 97 mbar (approx. 4–71 mmHg). To provide a better understanding of the vessel perfusion, we conducted flow experiments using a custom-made PDMS chamber (Fig. 6G). These tests confirmed the hollow structure of the printed vessels with continuous and smooth walls [16,97]. To assess permeability, we tracked the diffusion of a blue dye solution through the vessel walls [16]. Uniform surface thickness across the vessel, as depicted in Fig. 5C - μCT, revealed no variation in permeability within the walls. Hydrogels for vessel engineering should resist hydraulic pressure to ensure continuous perfusion [89]. Despite the permeable nature of the material, it comprises interpenetrating polymer networks that reinforce the entire structure, allowing it to withstand the directional flow of the medium. The pressure that caused the bursting of the 3D printed vessels reached 283.3 ± 39.97 mbar (above atmospheric pressure) at the fluid feeder (SI, S2, Supplementary video, n = 6), corresponding to a flow rate of 2.5 mL/min. Cui et al. noted similar burst pressures when testing similarly sized artificial vessels [51]. The reported pressure at burst is based on the readings of the pressure controller.

3.8. Cell adhesion and growth

PEG-Tyr accounted for the elasticity of the formed vessels and the GelMA fine-tuned the hydrogel-cell interactions. Gelatin and its derivatives contain native RGD adhesion motifs and therefore are preferred materials in regenerative applications [100]. To assess the biomaterials' properties *in vitro*, we used the EA.hy926 transformed EC line. All tested hydrogels showed cytocompatibility (Fig. 7A–C, SI, Figure S7). The Live/Dead staining results revealed a few dead cells (Fig. 7A and B and SI, Figure S6 A, B), reassuring their high viability assessed via metabolic activity-based assay (Fig. 7C). After 24 h of the culture, both the PEG0-gel and PEG2-gel showed approximately 80 % of metabolically active cells. However, on day 3, PEG2-gel showed a significant increase in total cell number, compared to the control samples. We hypothesize that PEG-Tyr enhances the overall hydrophilicity of the hydrogel, accounting for high cell viability and cell-colonization of the printed structure.

Cell studies, along with degradation test (Section 3.5), showed that the developed hydrogels may also further serve as an efficient platform for cell encapsulation. This is because the non-crosslinked MC dissolves and is cleared from the vessel scaffold's volume in the initial days after implantation, resulting in a space for better cell-cell interaction [71]. To verify the material's ability to integrate with the existing host tissue blood vessel network, CAM assays were conducted [47,101] (Fig. 7F–H). Following the two days of incubation, PEG0-gel and PEG2-gel samples did not show any cytotoxic effect on the blood vessel formation and embryo growth, compared to the CAMs development of eggs that were not subjected to any material. Representative photos of CAMs and their binary conversions, analyzed with ImageJ [102] are illustrated in Fig. 7F–H. Angiogenesis supporting properties of gel and PEG2-gel can be seen in an increase of vessel length and area occupied after 48 h incubation, compared to the control (Fig. 7I and J). Vessels grew on a significantly higher area for the PEG2-gel treated sample after 48 h. compared to the control. Furthermore, an insignificant increase was observed in the number of branching points in the vasculature that developed for PEG2-gel compared to gel and control (Fig. 7K), which may suggest that lower stiffness of the hydrogel with PEG can aid angiogenic events [69]. For all conditions, a progressive decrease in the vessels' thickness was noted, as the incubation continued, reflecting the extensive vasculogenesis and angiogenesis during embryonic development [47,48]. This agrees with previous studies showing that gelatin-containing materials may beneficially impact new tissue development, including the process of angiogenesis [103]. The cell viability and staining results, combined with CAM development studies, showed the potential of the developed hydrogel for studies involving vascularization.

EA.hy926 cells adhered to the PEG2-gel surface as observed in SEM images (Fig. 8A and B). Apart from the surface, cells on a PEG2-gel vessel highly populated the lumen entry after 7 days of culture (Fig. 8B). EA.hy926 cells, seeded by perfusion of cell suspension and statically cultured on the inner and outer wall of the hydrogel channels (Fig. 8C) [4] after 1 week of culture, were abundantly attached to the surface of the vessel (Fig. 8E and F). Blue nuclei staining with Hoechst (SI, Figure S8 A) patterned the vessel lumen when a cross-section was performed. The green staining of the cytoskeleton revealed good morphology of cells with pronounced focal adhesion sites [104] towards the hydrogel surface (Fig. 8F). This was further verified by confocal images (SI, Figure S8C, D) showing vessel arch with nuclei of the anchored cells.

Additionally, the vessel cross-section (Fig. 8D and SI, Figure S8 B) revealed cells infiltrating voids in the vessel wall, entering the lumen from the exterior of the vessel. The high porosity and sponge-like structure of the vessel wall, as shown in SEM images, facilitate ECs travel through the pores of hydrogel easing channel endothelialization [78]. Therefore, we believe that coaxial printing in combination with our hydrogel can facilitate angiogenesis processes due to the geometry mimicking capillary structures, helping ECs cells to organize and create a lumen [98,105–107].

3.9. In vivo studies - subfascial implantation in rat model and hydrogel testing

The implanted hydrogel material, both PEG0-gel and PEG2-gel did not affect the rat's activity after surgery (assessed by the Grimace scale and weight measurements presented in Fig. 9D). The implantation procedure for control (glass fiber) and the hydrogel are depicted in Fig. 9A–C. There was no loss of animals throughout the procedure and after sub-fascia implantation, and all animals had a positive recovery. At each time point (10, 20 and 30 days post subfascial implantation), the dorsal region was shaved, and a square patch of skin was removed (Fig. 9E and F, top panel) for macroscopic observation of the implanted hydrogels. The implanted hydrogels after 10 days post-surgery caused no significant tissue response, neither with signs of necrosis nor infection. There were no signs of inflammation or hematoma due to trauma of the incision and the hydrogel pouches are still visible. At 20 days post-subfascial implantation, healthy tissue can be observed with no visible

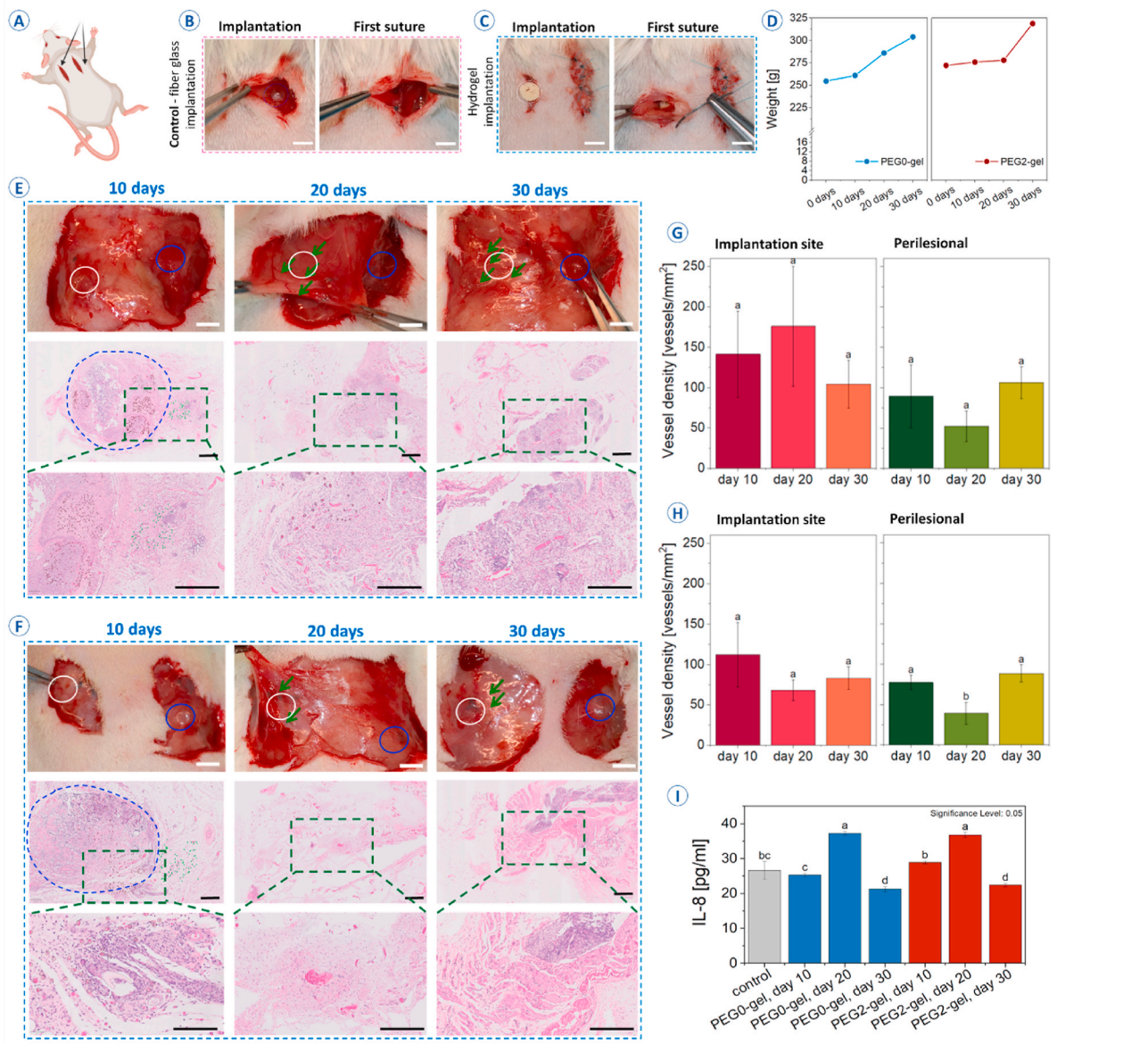

Fig. 9. A) Schematic representation of the incisions made for material implantation; Process of the B) fiber glass implantation (serving as experiment control), C) hydrogel implantation (scale bars correspond to 5 mm); D) Rat's weight measurements at each time point of the experiment; Implantation site of E) PEG2-gel, F) PEG0-gel, upon the removal of dorsal skin after 10, 20, 30 days (scale bars correspond to 5 mm), with corresponding H&E histological staining revealing newly formed blood vessels at the implantation site and perilesional, implanted hydrogel area is marked in blue (scale bars correspond to 800 μm); Vessel density for G) PEG2-gel and H) PEG0-gel at each time point of the experiment (in shades of red – vessel density at the implantation site, in green – perilesional); I) Levels of IL-8 evaluated at each time point of the experiment.

hydrogels onto the implantation site, but with the presence of detectable blood vessels (Fig. 9E and F), more highlighted in the case of PEG2-gel than the PEG0-gel or glass fiber (negative control). The same trend was observed after 30 days post-implantation when the vascular vessels occupied the entire implantation site when compared with the initial area. At the macroscopic level, the embedded hydrogels promoted vascularization of the subfascial layer.

The histological evaluation denoted at 10 days post-implantation showed a granulomatous inflammatory response for both samples, characterized by macrophages, epithelioid cells, and multinucleated giant cells.

Histological analysis showed areas of inflammatory edema, congestion, fibrin infiltrate rich in leukocytes (neutrophils, macrophages, lymphocytes, histiocytes), and fibrinous exudation for PEG0-gel and PEG2-gel. These processes were unnoticeable in the blood serum, as indicated by the determined IL-8 levels.

The reaction was diminished after 20 and 30 days, respectively, when the hydrogels were infiltrated with lymphocytes, macrophages, giant cells, and just a few fibroblasts (Fig. 9E and F, middle and bottom panels).

At 20 days, the inflammatory process persisted, but was less pronounced than at 10 days. Cellular and fibrinous exudations were reduced, with decreased congestion, edema, fibrinous exudation, and leukocyte influx. Condensed inflammatory cells, mainly rare macrophages, and fibroblasts, were identified in the tissue matrix, primarily associated with microcirculation congestion and diffuse edema. A minor edema area was observed at 30 days post-implantation, along with connective tissue neogenesis (fibroblasts and collagen fibers) and neoformation of blood vessels.

The microvessel density (Fig. 9G and H), was higher in the PEG2-gel-implanted group (141.25 vessels/mm^2) than that of the PEG0-gel group (121.20 vessels/mm^2) at 10 days post-implantation, suggesting that

hydrogels containing PEG were effective at promoting the vascularization among the groups. The number of perilesional blood vessels counted on HE staining images was lower than on the implanted site for both materials (PEG2-gel = 88.33 vessels/mm^2, PEG0-gel = 77.33 vessels/mm^2), suggesting that the scaffolds did not impact the area. At 20 days, an improved vascularization could be noted at the implanted site due to the scaffold integration into the connective tissue (PEG2-gel = 176 vessels/mm^2, PEG0-gel = 67.67 vessels/mm^2). The number of the perilesional blood vessels reached equilibrium for both scaffolds (PEG2-gel = 52.33 vessels/mm^2, PEG0-gel = 39.33 vessels/mm^2). After 30 days post-implantation, when the scaffolds were fully integrated into the implanted tissues, the number of counted blood vessels began to equalize between groups (PEG2-gel = 104.16 vessels/mm^2, PEG0-gel = 106.33 vessels/mm^2). The similar values for both scaffolds suggested that the recruitment of new vessels from pre-existing vessels was settled at this point, but still ongoing in the surrounding (perilesional) tissues (PEG2-gel = 83.00 vessels/mm^2, PEG0-gel = 88.67 vessels/mm^2), as the increase was observed compared with 20 days. Although a significant difference was found in the HE analysis of the number of blood vessels on the two scaffolds at different time points, new studies are needed to draw clear conclusions in this regard.

The levels of IL-8 (Fig. 9I) were used to evaluate the response of the immune system of the rats upon the hydrogel implantation. The serum IL-8 level showed relatively no differences between experimental and control sites in all time points except day 20 when the levels of IL-8 on both hydrogel types (PEG0-gel and PEG2-gel) rise by 38–39 % compared with control. This suggests that the compounds discharged from the hydrogels might cause the release of inflammatory mediators in the blood serum. The IL-8 level decreased up to 30 days post-surgery to a value similar to the control group.

4. Conclusions and future outlook

The fabrication of a vascular network for tissue engineering remains a great challenge. This is mainly due to the intricate nature of the blood vessel structure and the restrictions associated with the biomaterials available to provide a biologically effective implant. In this work, flexible vessel-like structures were coaxially 3D printed. The PEG2-gel has potential in the context of vascular tissue regeneration and printed vessels showed higher flexibility and elasticity than the one printed from PEG0-gel. Vessels maintained mechanical stability during and after printing, showed biocompatibility, and rendered cell adhesion and proliferation. Further optimizations and investigations are necessary to fully exploit the therapeutic potential and clinical translation of these fabricated vessels. A possible strategy for supporting the formation of nutrient and oxygen-carrying channels would be to prevascularize scaffolds before implantation by culturing them with the cells of interest. There is a persisting need for improved biomaterials with enhanced mechanical strength, biocompatibility and degradation characteristics. In addition, achieving precise control over microvascular architecture, especially in larger-scale constructs, remains a challenge. The accurate measurement of vessels burst pressure is challenging as the involved parameters such as pressure increase rate, the variations in methods to apply the pressure varies and a standard method can be developed in future. Moreover, scalability and the translation of 3D-printed vascular constructs to clinical applications necessitate addressing regulatory, ethical, and standardization issues. Our next steps will include exploring methods to integrate small-diameter vessels created using our approach with tissue constructs. Another point of interest should be the implementation of bioprinting techniques that enable the simultaneous printing of vascular-like constructs and tissue-specific matrix scaffolds.

Funding

This research work was supported by an Aspirant fellowship from the Fonds National de la Recherche Scientific de Belgique (FNRS) (grant number 46599, 2022 awarded to Julia Siminska-Stanny). A.S. acknowledges FNRS for providing a Research Credit (CDR) with grant number J.0188.24. M.H. acknowledges the financial support of Wallonia Brussels Internation (WBI).

Institutional review board statement

Not applicable.

Informed consent statement

Not applicable.

CRediT authorship contribution statement

Julia Simińska-Stanny: Writing – review & editing, Writing – original draft, Visualization, Validation, Methodology, Investigation, Formal analysis, Data curation, Conceptualization. **Lise Nicolas:** Formal analysis. **Adam Chafai:** Writing – review & editing, Methodology. **Hafez Jafari:** Writing – review & editing, Methodology. **Maryam Hajiabbas:** Writing – review & editing. **Gianina Dodi:** Writing – review & editing, Methodology, Investigation, Formal analysis. **Ioannis Gardikiotis:** Writing – review & editing. **Christine Delporte:** Writing – review & editing, Validation, Supervision, Resources, Methodology. **Lei Nie:** Writing – review & editing, Validation. **Daria Podstawczyk:** Writing – review & editing, Validation, Supervision, Conceptualization. **Amin Shavandi:** Writing – review & editing, Validation, Supervision, Resources, Project administration, Conceptualization.

Declaration of competing interest

The authors declare no conflict of interest.

Acknowledgments

The graphical abstract and Fig. 1, Fig. 8C and Fig. 9A were created with BioRender.com.

J.S.S. gratefully acknowledge the support by a grant from the FNRS (FNRS-Aspirant, Grant No. FC 46599), L.N. (Lise Nicolas) visiting master student – BRUFACE program. Lei Nie acknowledges the support from the Key Scientific Research Projects of Higher Education Institutions in Henan Province (24A430034). D.P. acknowledges the support from the Academia Iuvenum, Wrocław University of Science and Technology.

We thank the TIPs laboratory and the Micro-milli service platform (ULB) for the access to their experimental facilities.

We would like to acknowledge Martyna Nizioł and Piotr Śledzik who helped with coaxial printing. Additionally, we would like to express our gratitude to Francoise Gregoire and Nargis Bolaky for their logistic and technical help with cell culture. For performing microtomography scans and analysis we would like to thank Valérie Vancauwenberghe and Bruker Belgium SA, Kontich, for access to their laboratory.

Appendix A. Supplementary data

Supplementary data to this article can be found online at https://doi.org/10.1016/j.bioactmat.2024.02.019.

References

[1] L. Moroni, et al., Biofabrication strategies for 3D in vitro models and regenerative medicine, Nat. Rev. Mater. 3 (5) (2018) 21–37.
[2] S. Heltmann-Meyer, et al., Gelatin methacryloyl is a slow degrading material allowing vascularization and long-term use in vivo, Biomed. Mater. 16 (6) (2021) 065004.
[3] L. Godwin, M.A. Tariq, J.S. Crane, Histology, Capillary, StatPearls, 2023.
[4] J. Nie, et al., Vessel-on-a-chip with hydrogel-based microfluidics, Small 14 (45) (2018) e1802368.

[5] A. Dellaquila, et al., *In* vitro strategies to vascularize 3D physiologically relevant models, Adv. Sci. 8 (19) (2021) 2100798.
[6] S.Y. Hann, et al., Recent advances in 3D printing: vascular network for tissue and organ regeneration, Transl. Res. 211 (2019) 46–63.
[7] B. Grigoryan, et al., Multivascular networks and functional intravascular topologies within biocompatible hydrogels, Science 364 (6439) (2019) 458–464.
[8] J. Lee, et al., Fabrication of microchannels and evaluation of guided vascularization in biomimetic hydrogels, Tissue Engineering and Regenerative Medicine 15 (4) (2018) 403–413.
[9] G. Tang, et al., Liquid-embedded (bio)printing of alginate-free, standalone, ultrafine, and ultrathin-walled cannular structures, Proc. Natl. Acad. Sci. USA 120 (7) (2023) e2206762120.
[10] J.P.K. Armstrong, et al., 3D bioprinting using a templated porous bioink, Adv. Healthcare Mater. 5 (14) (2016) 1724–1730.
[11] D. Podstawczyk, et al., Coaxial 4D Printing of Vein-Inspired Thermoresponsive Channel Hydrogel Actuators, Adv. Funct. Mater. (2023) 2310514.
[12] S. Kawara, et al., Capillary-scale hydrogel microchannel networks by wire templating, Small 19 (42) (2023) 2301163.
[13] W. Jia, et al., Direct 3D bioprinting of perfusable vascular constructs using a blend bioink, Biomaterials 106 (2016) 58–68.
[14] T. Shyam Mohan, et al., 3D coaxial bioprinting: process mechanisms, bioinks and applications, Prog. Biomed. Eng. 4 (2) (2022) 022003.
[15] G. Gao, et al., Tissue engineered bio-blood-vessels constructed using a tissue-specific bioink and 3D coaxial cell printing technique: a novel therapy for ischemic disease, Adv. Funct. Mater. 27 (33) (2017) 1700798.
[16] X. Zhou, et al., 3D-bioprinted vascular scaffold with tunable mechanical properties for simulating and promoting neo-vascularization, Smart Materials in Medicine 3 (2022) 199–208.
[17] B. Böttcher, et al., 3D bioprinting of prevascularized full-thickness gelatin-alginate structures with embedded Co-cultures, Bioengineering 9 (6) (2022) 242.
[18] Y.S. Zhang, Q. Pi, A.M. van Genderen, Microfluidic bioprinting for engineering vascularized tissues and organoids, J. Vis. Exp. (126) (2017).
[19] J. Liang, et al., Hybrid hydrogels based on methacrylate-functionalized gelatin (GelMA) and synthetic polymers, Biomedical Materials & Devices 1 (1) (2023) 191–201.
[20] R. Kaufmann, et al., Vascular 3D printing with a novel biological tissue mimicking resin for patient-specific procedure simulations in interventional radiology: a feasibility study, J. Digit. Imag. 35 (1) (2022) 9–20.
[21] Isik, M., et al., 3D printing of extracellular matrix-based multicomponent, all-natural, highly elastic, and functional materials toward vascular tissue engineering. Adv. Healthcare Mater.. n/a(n/a): p. 2203044.
[22] Carrabba, M., et al., Development of a novel hierarchically biofabricated blood vessel mimic decorated with three vascular cell populations for the reconstruction of small-diameter arteries. Adv. Funct. Mater.. n/a(n/a): p. 2300621.
[23] S. Li, , et al.Anticoagulative Bioinspired, 19F MRI-visualizable bilayer hydrogel tubes as high patency small-diameter vascular grafts, Small 19 (42) (2023) 2302621.
[24] S.Y. Hann, et al., 3D printed biomimetic flexible blood vessels with iPS cell-laden hierarchical multilayers, Biomedical Engineering Advances 4 (2022) 100065.
[25] E. Jalalvandi, A. Shavandi, Shear thinning/self-healing hydrogel based on natural polymers with secondary photocrosslinking for biomedical applications, Journal of the Mechanical Behavior of Biomedical Materials 90 (2019) 191–201. ISSN 1751-6161.
[26] J. Li, et al., Development and systematic characterization of GelMA/alginate/PEGDMA/xanthan gum hydrogel bioink system for extrusion bioprinting, Biomaterials 293 (2023) 121969.
[27] P. Kim, et al., Fabrication of poly(ethylene glycol): gelatin methacrylate composite nanostructures with tunable stiffness and degradation for vascular tissue engineering, Biofabrication 6 (2) (2014) 024112.
[28] Y. Piao, et al., Biomedical applications of gelatin methacryloyl hydrogels, Engineered Regeneration 2 (2021) 47–56.
[29] C.B. Hutson, et al., Synthesis and characterization of tunable poly(ethylene glycol): gelatin methacrylate composite hydrogels, Tissue Eng. 17 (13–14) (2011) 1713–1723.
[30] A.A. Aldana, et al., Development of 3D bioprinted GelMA-alginate hydrogels with tunable mechanical properties, Bioprinting 21 (2021) e00105.
[31] L. Xu, et al., Bioprinting small diameter blood vessel constructs with an endothelial and smooth muscle cell bilayer in a single step, Biofabrication 12 (4) (2020) 045012.
[32] H.Y. Jung, et al., Tunable and high tissue adhesive properties of injectable chitosan based hydrogels through polymer architecture modulation, Carbohydr. Polym. 261 (2021) 117810.
[33] J. Zhu, Bioactive modification of poly(ethylene glycol) hydrogels for tissue engineering, Biomaterials 31 (17) (2010) 4639–4656.
[34] J. Simińska-Stanny, et al., Optimizing phenol-modified hyaluronic acid for designing shape-maintaining biofabricated hydrogel scaffolds in soft tissue engineering, Int. J. Biol. Macromol. (2023) 244.
[35] I.A. Barroso, et al., Photocurable GelMA adhesives for corneal perforations, Bioengineering 9 (2) (2022).
[36] R. Goto, et al., Gelatin methacryloyl-riboflavin (GelMA-RF) hydrogels for bone regeneration, Int. J. Mol. Sci. 22 (4) (2021) 1635.
[37] T. Liu, et al., *Corrigendum to "Porcupine-inspired microneedles coupled with an adhesive back patching as dressing for accelerating diabetic wound healing"* [Acta Biomaterialia Volume 160, 1 April 2023, Pages 32-44], Acta Biomater. 171 (2023) 580.
[38] K. Park, et al., In situ cross-linkable gelatin–poly(ethylene glycol)–tyramine hydrogel via enzyme-mediated reaction for tissue regenerative medicine, J. Mater. Chem. 21 (2011) 13180–13187.
[39] A. GhavamiNejad, et al., Crosslinking strategies for 3D bioprinting of polymeric hydrogels, Small 16 (35) (2020) 2002931.
[40] Q. Gao, et al., Coaxial nozzle-assisted 3D bioprinting with built-in microchannels for nutrients delivery, Biomaterials 61 (2015) 203–215.
[41] R. Taymour, et al., 3D bioprinting of hepatocytes: core–shell structured co-cultures with fibroblasts for enhanced functionality, Sci. Rep. 11 (1) (2021) 5130.
[42] B. Velasco-Rodriguez, et al., Hybrid methacrylated gelatin and hyaluronic acid hydrogel scaffolds. Preparation and systematic characterization for prospective tissue engineering applications, Int. J. Mol. Sci. 22 (13) (2021) 6758.
[43] M.-N. Labour, et al., Development of 3D hepatic constructs within polysaccharide-based scaffolds with tunable properties, Int. J. Mol. Sci. 21 (2020) 3644.
[44] S. Taheri, et al., Injectable, pore-forming, perfusable double-network hydrogels resilient to extreme biomechanical stimulations, Adv. Sci. 9 (2) (2022) e2102627.
[45] H. Jafari, et al., Ovarian cell encapsulation in an enzymatically crosslinked silk-based hydrogel with tunable mechanical properties, Gels 7 (3) (2021).
[46] Y. Altun, et al., Visualizing H2O2 and NO in Endothelial Cells: Strategies and Pitfalls, 2023.
[47] H. Jafari, et al., An injectable, self-healing, 3D printable, double network co-enzymatically crosslinked hydrogel using marine poly- and oligo-saccharides for wound healing application, Appl. Mater. Today 29 (2022) 101581.
[48] G. Merckx, et al., Chorioallantoic membrane assay as model for angiogenesis in tissue engineering: focus on stem cells, Tissue Eng. B Rev. 26 (6) (2020) 519–539.
[49] L. Faihs, et al., A novel artificial intelligence-based approach for quantitative assessment of angiogenesis in the ex ovo CAM model, Cancers 14 (17) (2022).
[50] M. Klarhöfer, et al., High-resolution blood flow velocity measurements in the human finger, Magn. Reson. Med. 45 (4) (2001) 716–719.
[51] H. Cui, et al., In vitro and in vivo evaluation of 3D bioprinted small-diameter vasculature with smooth muscle and endothelium, Biofabrication 12 (1) (2019) 015004.
[52] M. Ho, et al., PEGylated poly(amidoamine) dendrimers-based drug loading vehicles for delivering carboplatin in treatment of various cancerous cells, J. Nanoparticle Res. (2019) 21.
[53] S. Kamyar, et al., Synthesis and characterization of polyethylene glycol mediated silver nanoparticles by the green method, Int. J. Mol. Sci. 13 (2012) 6639–6650.
[54] F. Askari, et al., Reduction in protein absorption on ophthalmic lenses by PEGDA bulk modification of silicone acrylate-based formulation, Progress in Biomaterials 8 (2019) 1–15.
[55] S. Cherevkov, et al., Interface chemical modification between all-inorganic perovskite nanocrystals and porous silica microspheres for composite materials with improved emission, Nanomaterials 11 (2021), https://doi.org/10.3390/nano11010119.
[56] M. Sarker, et al., Influence of ionic crosslinkers (Ca(2+)/Ba(2+)/Zn(2+)) on the mechanical and biological properties of 3D Bioplotted Hydrogel Scaffolds, J. Biomater. Sci. Polym. Ed. 29 (10) (2018) 1126–1154.
[57] Horseradish peroxidase-catalyzed crosslinking of fibrin microthread scaffolds, Tissue Eng. C Methods 26 (6) (2020) 317–331.
[58] Z. Żołek-Tryznowska, 6 - rheology of printing inks, in: J. Izdebska, S. Thomas (Eds.), Printing on Polymers, William Andrew Publishing, 2016, pp. 87–99.
[59] G. Kimbell, M.A. Azad, Chapter FIFTEEN - 3D printing: bioinspired materials for drug delivery, in: M. Nurunnabi (Ed.), Bioinspired and Biomimetic Materials for Drug Delivery, Woodhead Publishing, 2021, pp. 295–318.
[60] Y. Sun, et al., Effects of plasticizer type and concentration on rheological, physico-mechanical and structural properties of chitosan/zein film, Int. J. Biol. Macromol. 143 (2020) 334–340.
[61] A. Domján, J.n. Bajdik, K. Pintye-Hódi, Understanding of the plasticizing effects of glycerol and PEG 400 on chitosan films using solid-state NMR spectroscopy, Macromolecules 42 (2009).
[62] B. Zhang, et al., Effects of polyethylene glycol on the flexibility of cold-setting melamine–urea–formaldehyde resin, European Journal of Wood and Wood Products 80 (2022).
[63] T. G.Mezger, in: A. Paar (Ed.), Applied Rheology with Joe Flow on Rheology Road, seventh ed. ed, Anton Paar, March 2020, p. 196, 7th edition.
[64] T. Gao, et al., Optimization of gelatin-alginate composite bioink printability using rheological parameters: a systematic approach, Biofabrication 10 (3) (2018) 034106.
[65] H. Wyss, et al., Biophysical properties of normal and diseased renal glomeruli, Am. J. Physiol. Cell Physiol. 300 (2010) C397–C405.
[66] Q. Pi, et al., Digitally tunable microfluidic bioprinting of multilayered cannular tissues, Adv. Mater. 30 (43) (2018) e1706913.
[67] H. Lei, et al., Stretchable hydrogels with low hysteresis and anti-fatigue fracture based on polyprotein cross-linkers, Nat. Commun. 11 (1) (2020) 4032.
[68] D. Wei, et al., Dynamically modulated core–shell microfibers to study the effect of depth sensing of matrix stiffness on stem cell fate, ACS Appl. Mater. Interfaces 13 (32) (2021) 37997–38006.
[69] J. Leonard-Duke, et al., Variations in mechanical stiffness alter microvascular sprouting and stability in a PEG hydrogel model of idiopathic pulmonary fibrosis, Microcirculation 30 (5–6) (2023) e12817.
[70] Q. Wei, et al., Soft hydrogels for balancing cell proliferation and differentiation, ACS Biomater. Sci. Eng. 6 (8) (2020) 4687–4701.
[71] T. Ahlfeld, et al., Methylcellulose – a versatile printing material that enables biofabrication of tissue equivalents with high shape fidelity, Biomater. Sci. 8 (8) (2020) 2102–2110.

[72] F. Mahler, et al., Blood pressure fluctuations in human nailfold capillaries, Am. J. Physiol. 236 (6) (1979) H888–H893.
[73] Q. Mu, T. Hu, J. Yu, Molecular insight into the steric shielding effect of PEG on the conjugated staphylokinase: biochemical characterization and molecular dynamics simulation, PLoS One 8 (7) (2013) e68559.
[74] S.S. Es-haghi, A.I. Leonov, R.A. Weiss, On the necking phenomenon in pseudo-semi-interpenetrating double-network hydrogels, Macromolecules 46 (15) (2013) 6203–6208.
[75] J. Nie, et al., Orientation in multi-layer chitosan hydrogel: morphology, mechanism and design principle, Sci. Rep. 5 (1) (2015) 7635.
[76] P.L. Thi, et al., In situ forming and reactive oxygen species-scavenging gelatin hydrogels for enhancing wound healing efficacy, Acta Biomater. 103 (2020) 142–152.
[77] R. Ziadlou, et al., Optimization of hyaluronic acid-tyramine/silk-fibroin composite hydrogels for cartilage tissue engineering and delivery of anti-inflammatory and anabolic drugs, Mater. Sci. Eng. C 120 (2021) 111701.
[78] C.B.S. Henry, B.R. Duling, Permeation of the luminal capillary glycocalyx is determined by hyaluronan, Am. J. Physiol. Heart Circ. Physiol. 277 (2) (1999) H508–H514.
[79] M. Lovett, et al., Vascularization strategies for tissue engineering, Tissue Eng. B Rev. 15 (2009) 353–370.
[80] Q. Chai, Y. Jiao, X. Yu, Hydrogels for biomedical applications: their characteristics and the mechanisms behind them, Gels 3 (1) (2017).
[81] J. Sievers, et al., Determination of hydrogel swelling factors by two established and a novel non-contact continuous method, J. Appl. Polym. Sci. 138 (18) (2021) 50326.
[82] V.G. Muir, J.A. Burdick, Chemically modified biopolymers for the formation of biomedical hydrogels, Chem. Rev. 121 (18) (2021) 10908–10949.
[83] Y. Wang, S. Zhang, D.S.W. Benoit, Degradable poly(ethylene glycol) (PEG)-based hydrogels for spatiotemporal control of siRNA/nanoparticle delivery, J. Contr. Release 287 (2018) 58–66.
[84] K. Schütz, et al., Three-dimensional plotting of a cell-laden alginate/methylcellulose blend: towards biofabrication of tissue engineering constructs with clinically relevant dimensions, Journal of Tissue Engineering and Regenerative Medicine 11 (5) (2017) 1574–1587.
[85] E.M. Brey, L.V. McIntire, 59 - vascular assembly in engineered and natural tissues, in: A. Atala, et al. (Eds.), Principles of Regenerative Medicine, Academic Press, San Diego, 2008, pp. 1020–1037.
[86] C.C. Chang, et al., Direct-write bioprinting three-dimensional biohybrid systems for future regenerative therapies, J. Biomed. Mater. Res. B Appl. Biomater. 98 (1) (2011) 160–170.
[87] X. Cui, et al., Advances in extrusion 3D bioprinting: a focus on multicomponent hydrogel-based bioinks, Adv. Healthcare Mater. 9 (15) (2020) 1901648.
[88] C.R. Alcala-Orozco, et al., Converging functionality: strategies for 3D hybrid-construct biofabrication and the role of composite biomaterials for skeletal regeneration, Acta Biomater. 132 (2021) 188–216.
[89] R. Xie, et al., Engineering of hydrogel materials with perfusable microchannels for building vascularized tissues, Small 16 (15) (2020) 1902838.
[90] J.C. Kohn, M.C. Lampi, C.A. Reinhart-King, Age-related vascular stiffening: causes and consequences, Front. Genet. 6 (2015) 112.
[91] M. Hospodiuk, et al., The bioink: a comprehensive review on bioprintable materials, Biotechnol. Adv. 35 (2) (2017) 217–239.
[92] C. Mandrycky, et al., 3D bioprinting for engineering complex tissues, Biotechnol. Adv. 34 (4) (2016) 422–434.
[93] D. Podstawczyk, et al., 3D printed stimuli-responsive magnetic nanoparticle embedded alginate-methylcellulose hydrogel actuators, Addit. Manuf. 34 (2020) 101275.
[94] K.Y. Lee, D.J. Mooney, Alginate: properties and biomedical applications, Prog. Polym. Sci. 37 (1) (2012) 106–126.
[95] K.A. Gold, et al., 3D bioprinted multicellular vascular models, Adv. Healthcare Mater. 10 (21) (2021) e2101141.
[96] Z. Zeng, et al., Coaxial-printed small-diameter polyelectrolyte-based tubes with an electrostatic self-assembly of heparin and YIGSR peptide for antithrombogenicity and endothelialization, Bioact. Mater. 6 (6) (2021) 1628–1638.
[97] S. Hong, et al., Coaxial bioprinting of cell-laden vascular constructs using a gelatin-tyramine bioink, Biomater. Sci. 7 (2019).
[98] A. Kjar, et al., Engineering of tissue constructs using coaxial bioprinting, Bioact. Mater. 6 (2) (2021) 460–471.
[99] C.M. Jones, et al., Measurement science in the circulatory system, Cell. Mol. Bioeng. 7 (1) (2014) 1–14.
[100] Y.-C. Chen, et al., Functional human vascular network generated in photocrosslinkable gelatin methacrylate hydrogels, Adv. Funct. Mater. 22 (10) (2012) 2027–2039.
[101] Y. Luo, et al., Hyaluronic acid facilitates angiogenesis of endothelial colony forming cell combining with mesenchymal stem cell via CD44/MicroRNA-139-5p pathway, Front. Bioeng. Biotechnol. 10 (2022).
[102] C.A. Schneider, W.S. Rasband, K.W. Eliceiri, NIH Image to ImageJ: 25 years of image analysis, Nat. Methods 9 (7) (2012) 671–675.
[103] L. Dreesmann, M. Ahlers, B. Schlosshauer, The pro-angiogenic characteristics of a cross-linked gelatin matrix, Biomaterials 28 (36) (2007) 5536–5543.
[104] A. Prasad, E. Alizadeh, Cell form and function: interpreting and controlling the shape of adherent cells, Trends Biotechnol. 37 (4) (2019) 347–357.
[105] S.C. Millik, et al., 3D printed coaxial nozzles for the extrusion of hydrogel tubes toward modeling vascular endothelium, Biofabrication 11 (4) (2019) 045009.
[106] S. Lei, et al., Directly coaxial 3D bioprinting of large-scale vascularized tissue constructs, Biofabrication 12 (2020).
[107] D. Gholobova, et al., Functional evaluation of prevascularization in one-stage versus two-stage tissue engineering approach of human bio-artificial muscle, Biofabrication 12 (3) (2020) 035021.